©2016. This manuscript version is made available under the CC-BY-NC-ND 4.0 license http://creativecommons.org/licenses/by-nc-nd/4.0/
DOI http://dx.doi.org/10.1016/j.rse.2016.02.036

SMOS INSTRUMENT PERFORMANCE AND CALIBRATION AFTER 5 YEARS IN ORBIT

M. Martín-Neira (1), R. Oliva (2), I. Corbella (3), F. Torres (3), N. Duffo (3), I. Durán (3), J. Kainulainen (4), J. Closa (5), A. Zurita (5), F. Cabot (6), A. Khazaal (6), E. Anterrieu (7), J. Barbosa (8), G. Lopes (8), J. Tenerelli (9), R. Díez-García (10), J. Fauste (2), F. Martín-Porqueras (11), V. González-Gambau (12), A. Turiel (12), S. Delwart (13), R. Crapolicchio (13), M. Suess (1)

Corresponding author

M. Martín-Neira and M. Suess are with ESA-ESTEC, Keplerlaan 1, 2200 AG Noordwijk, The Netherlands. (e-mail: manuel.Martín-Neira@esa.int)

Authors' affiliations

(1) European Space Agency at ESTEC, Noordwijk, The Netherlands.
(2) European Space Agency at ESAC, Villanueva de la Cañada, Spain.
(3) Polytechnic University of Catalonia (UPC), Barcelona, Spain.
(4) Harp Technologies Ltd., Espoo, Finland.
(5) EADS-CASA Espacio, Madrid, Spain.
(6) Centre d'Etudes Spatiales de la BIOsphère (CESBIO), Toulouse, France.
(7) Institut de Recherche en Astrophysique et Planétologie (IRAP), Toulouse, France.
(8) DEIMOS, Lisbon, Portugal.
(9) OceanDataLab, Brest, France.
(10) IDEAS, ESAC, Villanueva de la Cañada, Spain.
(11) VEGA Telespazio, ESAC, Villanueva de la Cañada, Spain.
(12) SMOS Barcelona Expert Centre, Barcelona, Spain.
(13) European Space Agency at ESRIN, Frascati, Italy.

Keywords

Soil Moisture and Ocean Salinity (SMOS) Mission, soil moisture, sea surface salinity, L-Band radiometry, aperture synthesis, MIRAS

1 Abstract

ESA's Soil Moisture and Ocean Salinity (SMOS) mission, launched 2-Nov-2009, has been in orbit for over 5 years, and its Microwave Imaging Radiometer with Aperture Synthesis (MIRAS) in two dimensions keeps working well. The calibration strategy remains overall as established after the commissioning phase, with a few improvements. The data for this whole period has been reprocessed with a new fully polarimetric version of the Level-1 processor which includes a refined calibration schema for the antenna losses. This reprocessing has allowed the assessment of an improved performance benchmark. An overview of the results and the progress achieved in both calibration and image reconstruction is presented in this contribution.

2 INTRODUCTION

With an experience of over 5 years of in-orbit operation, much has been learnt on how MIRAS works and how its observations can be improved through better calibration and image reconstruction techniques. The purpose of this paper is to update the reader with the latest results on the payload performance and data processing of the SMOS mission (Mecklenburg et al., 2012). SMOS is currently delivering several products, some of them used by operational systems, others only for scientific research (Mecklenburg et al., in press). MIRAS is a Microwave Imaging Radiometer with two-dimensional Aperture Synthesis, which remains being the first and so far, the only one of its kind, in space. The main feature of MIRAS is that it obtains two-dimensional images at every snapshot without needing any mechanical scanning of its antenna, a very distinct capability when compared with traditional scanners or push-broom radiometers. A detailed description of the instrumental aspects of MIRAS can be found in (McMullan et al., 2008) while the on-board Calibration System and respective in-flight calibration strategy are described in (Brown et al., 2008) and (Martín-Neira et al., 2008). One year after launch the calibration approach was slightly modified with the initial flight experience, and the first SMOS instrument in-orbit performance was assessed in (Oliva et al., 2013), including the effect of the unexpectedly severe Radio Frequency Interference from ground transmitters (Oliva et al., 2012). The present paper will then follow the same structure as (Oliva et al., 2013), with important

additions brought by the accumulated experience of over 5 years: Section 3 provides an overview of the main sources of error and the current mitigation strategies used to overcome them; Section 4 summarizes the current status of calibration activities, including all latest modifications to the initial calibration plan; Section 5 presents the in-orbit behaviour of the most critical instrument parameters; Section 6 gives the performance obtained with the latest version of the Level-1 processor, through the spatial and temporal analysis of brightness temperature images, and finally, Section 7 includes a view on the current investigations that should lead to the next version of the Level-1 processor with a hint on the expected improvements.

It is worth mentioning that, at the time of the writing of this paper, the running version of the operational SMOS Level-1 data processor is V620, that a new version, V700, has been delivered and is under assessment, and that the entire data record of the SMOS mission (from January 2010 onwards) has been reprocessed with V620 and is available to the whole SMOS user community.

3 ERROR SOURCES AND MITIGATION TECHNIQUES

3.1 Error Sources

Different error sources cause different effects on the SMOS brightness temperature images. Therefore in this section the error sources will be presented according to the effect they produce in the images.

3.1.1 Systematic Spatial Ripple

Figure 1 presents the deviation, with respect to a forward model, of an image of the brightness temperature measured by SMOS over a portion of the South-Eastern Pacific Ocean in X-polarization (X-polarization refers to the image formed with the signal collected by the horizontal probe of MIRAS antenna elements). The comparison is performed after averaging many snapshots so that random errors induced by the radiometric resolution can be neglected, and only systematic errors remain. The most prominent features of such deviation image are a +0.96 K bias and a 1.5 K rms spatial ripple, both statistics evaluated within the dashed circle shown in Figure 1. Similar statistics can be computed for

the Y-polarization as well as for the Stokes-3 and Stokes-4 parameters, obtaining, in general, different values for the different parameters, values which, in turn, depend on the particular image reconstruction approach being applied, that is, on the Level-1 processor version. Furthermore, and although it is not as easy to show as with measurements of the relatively uniform ocean, bias and ripples also appear in images acquired over any region of the Earth, be it land, ice or coastlines, and over the Cold Sky, exhibiting a magnitude which is scene-dependent. Interpreting the bias as a spatial ripple of an infinite spatial wavelength, both bias and spatial ripple shall be understood as comprised within the 'spatial ripple' referred to in what follows.

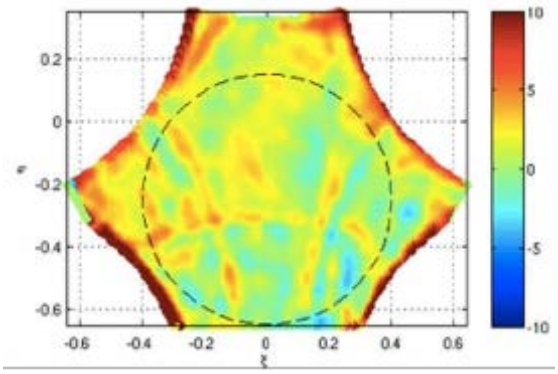

Figure 1: Example of bias and spatial ripples of SMOS images when compared to **a radiative transfer** ocean model. **The axes are the director cosines and the colour scale is in Kelvin.**

The cause and existence of the systematic spatial ripple underlying all SMOS images was already studied before SMOS launch (Camps et al., 2005)(Anterrieu, 2007). Thanks to the investigations conducted during the last 5 years in several directions, using flight data, an important conclusion has been consolidated: the spatial ripple results mostly from the combination of having different antenna element patterns and imaging in alias conditions (that is, using a spatial sampling which leads to having aliased images in some parts of the real space). This is illustrated in Figure 2, which shows a similar deviation image to Figure 1 obtained simulating different conditions: the left and right columns assume identical and different –perfectly known– antenna patterns respectively, while the rows correspond to different antenna element spacings, the one of MIRAS (0.875λ) in the top, and another one which is alias-free (0.55λ) in the bottom. As it is evident, the spatial ripple appears only in the top right plot, that

is, for alias condition and different antenna patterns. If there is no aliasing, or/and if the antenna patterns are all identical, then there is no significant spatial ripple.

As a consequence of this, two further results have now been well established: first, even in the ideal case where the antenna pattern of every antenna element were known perfectly well, a non-negligible systematic spatial error would still be present in SMOS images, dubbed ‘noise floor’; second, the part of the scene outside the alias-free area does have an impact on the scene recovered in the alias-free region, or in other words, the spatial ripple in the alias-free area depends on the scene in the aliased regions (Corbella et al., 2014).

The first result might be the most striking one, since for long, it had been expected that the accurate knowledge of the antenna patterns, very carefully characterized on ground and used in the image reconstruction, would have enabled the acquisition of images with negligible ripple. It also emphasizes the need of having the interferometric instrument with either an alias-free element spacing or as similar antenna patterns as possible, to suppress the spatial ripple from the images. The second result, on the other hand, has been the basis to build ripple reduction methods to improve the current SMOS images, as will be seen in the section devoted to mitigation techniques below. Finally the contribution to the spatial ripple due to the limited knowledge of the antenna patterns and residual calibration errors shall not be forgotten.

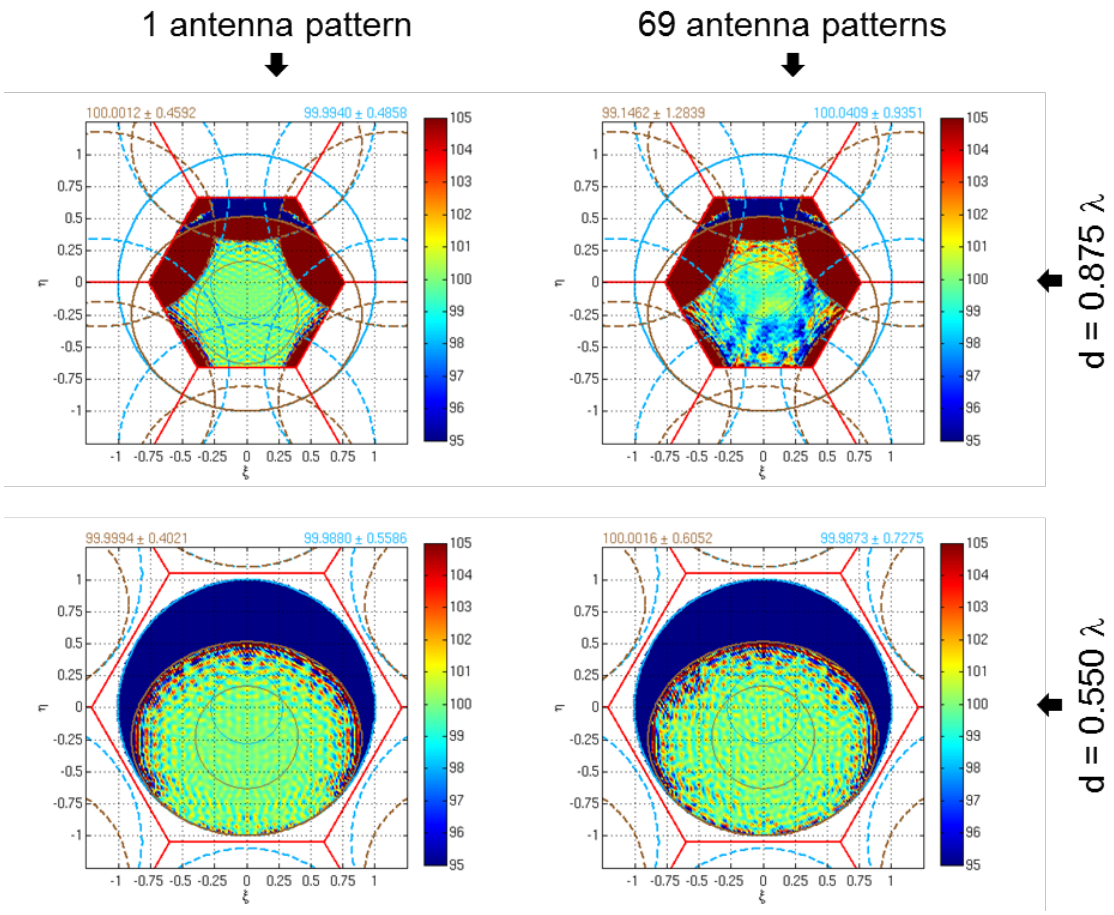

Figure 2: Illustration that the spatial ripple results from the combination of different antenna patterns and alias condition. **The image shows the Earth and the sky at a spatially uniform but different brightness temperature, viewed with the nominal SMOS geometry. The axes are the director cosines and the colour bar represents the retrieved brightness temperature in Kelvin.**

3.1.2 Sun and RFI Tails

Figure 3 is a deviation image as Figure 1 but acquired at a time when the Sun is in front of the antenna. The Sun can be seen as a white circle towards the right side of the unity circle, which represents the front hemisphere of the antenna. The area shaded in blue is the locus of possible positions of the Sun as seen from the SMOS orbit around the year. The Sun locus is sufficiently far away from the extended field of view of SMOS that it would not cause any ripples if it were not because of the aliasing and the side lobes. Indeed, a replica of the Sun is clearly visible inside the field of view. Moreover, the real Sun and its replica appear connected by lines of side lobes which cross the entire field of view, including the alias free region. Extending the lines of side lobes through the black dashed lines it is possible to

located a second alias in the upper part of the unity circle, outside the extended alias-free field of view. The cause of these side lobes is the same as that of the spatial ripple: the differences across antenna patterns enhance the side lobes joining the Sun aliases, which are generated by the element spacing. Patterns of side lobes are also excited by Radio Frequency Interference (RFI) transmitters, which behave within the image reconstruction process, much in the same way as the Sun. This is illustrated in Figure 4, where the extended alias-free field of view is projected on ground at a location of an RFI source: an hexagonal pattern of side lobes is clearly visible. RFI sources remain being an important error source in SMOS (Oliva et al., in press).

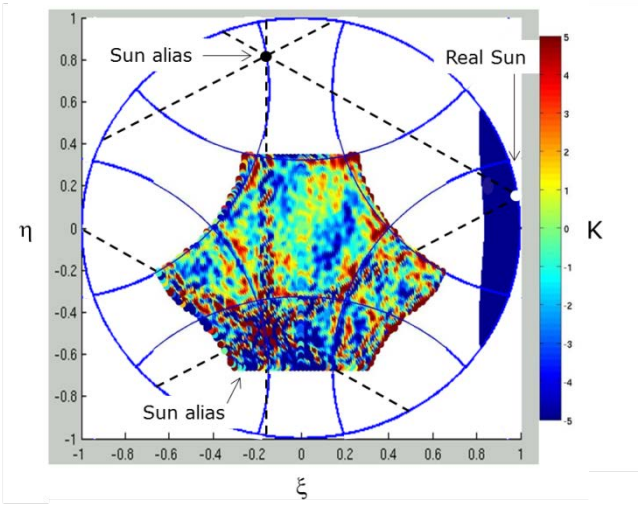

Figure 3: Sun tails and alias affecting an ocean image

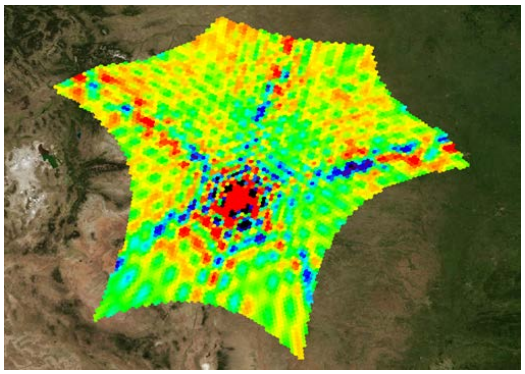

Figure 4: Hexagonal pattern of side lobes excited by a strong Radio Frequency Interference source

3.1.3 Land-Sea Contamination

The left plot of Figure 5 shows a global view of the oceans with the accumulated deviation of SMOS measurements from a forward model. Brightness temperature warmer than the model are **seen** around all continental masses which wrongly lead to fresher water retrievals. This feature of SMOS images is referred to as 'land-sea contamination' and is of concern among the Sea Surface Salinity community because it can extend several hundreds of kilometers into the open ocean. Much effort has been devoted to understand the reason behind this land-sea contamination. The current understanding is that it is caused by several contributions. The most important one seems to be a calibration error, of the order of 2%, in the amplitude of the correlations, the so-called G_{kj} correlator efficiency coefficients (Corbella et al., in press). Although this problem with the correlation coefficients has been identified, to date, the root cause has not been found yet and the search within the instrumental details related to it continues. The second contributor is the spatial ripple described above, generated by the warmer land and extending into the ocean.

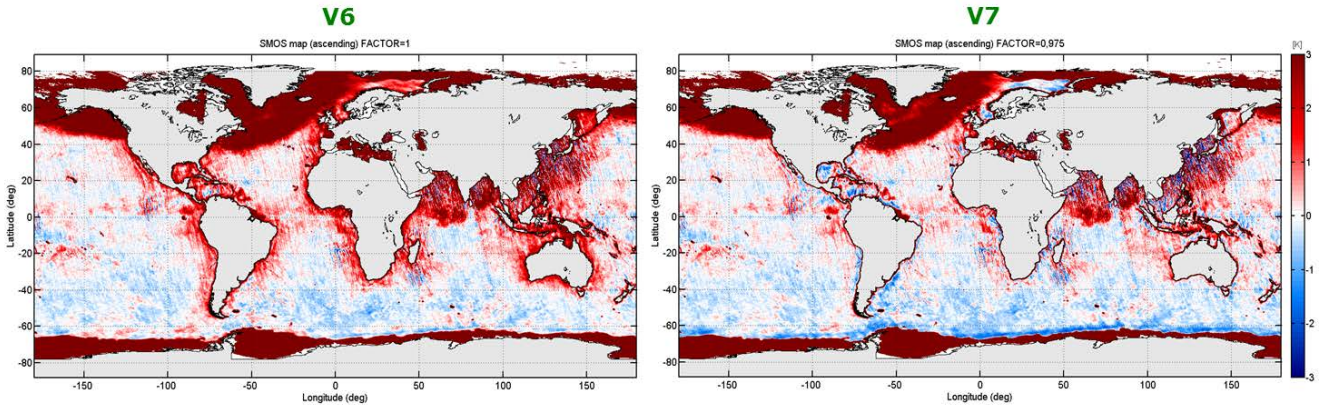

Figure 5: **Stokes-1/2 residual images against a radiative transfer ocean model using present correlation efficiency factors (left), where the land-sea contamination is clearly observed around the continental masses, and using corrected values (right), with significantly reduced errors. The warm areas around Alaska, Greenland, Arabian Sea, Gulf of Bengal and Sea of China are due to Radio Frequency Interference, and the blue rim around Antarctica is due to un-modelled sea ice.**

3.1.4 Seasonal Variations

The right plot of Figure 6 shows the current deviation of the Stokes-1/2 parameter over the Pacific Ocean, averaged within the alias-free field of view, with respect to an ocean model, along the descending passes. The plot spans 5 years, from 2010 till 2014, and from **60° South to 60° North** in

latitude, with a brightness temperature scale of ±1.2 K. This **Hovmöller** plot constitutes a powerful tool to analyze any seasonal (and latitudinal) variations. Besides the red stripe during the Commissioning Phase in early 2010, the variations are contained within ±0.4 K except for the eclipse periods **(mid-November to mid-February)** and a region around October where some warm signatures are observed. During an eclipse, the Sun, which can be as high as 31° above the antenna horizon, is suddenly occulted by the Earth. The antenna skin temperature falls down a couple of tens of degrees, from around 28°C to some 5°C. When the satellite exists the Earth shadow, the Sun warms up the antenna again until it reaches the temperature it would have if there had been no eclipse. This post-eclipse transient causes, in every descending orbit, a warm anomaly in the brightness temperature which extends to latitudes as low as 30° North. On the other hand, the reason for the October warm anomaly has not yet been uncovered. Attempts to correlate it with residual galactic noise or other geophysical signatures have failed and hence, an instrumental origin should be assumed. Furthermore this anomaly seems more intense in 2014.

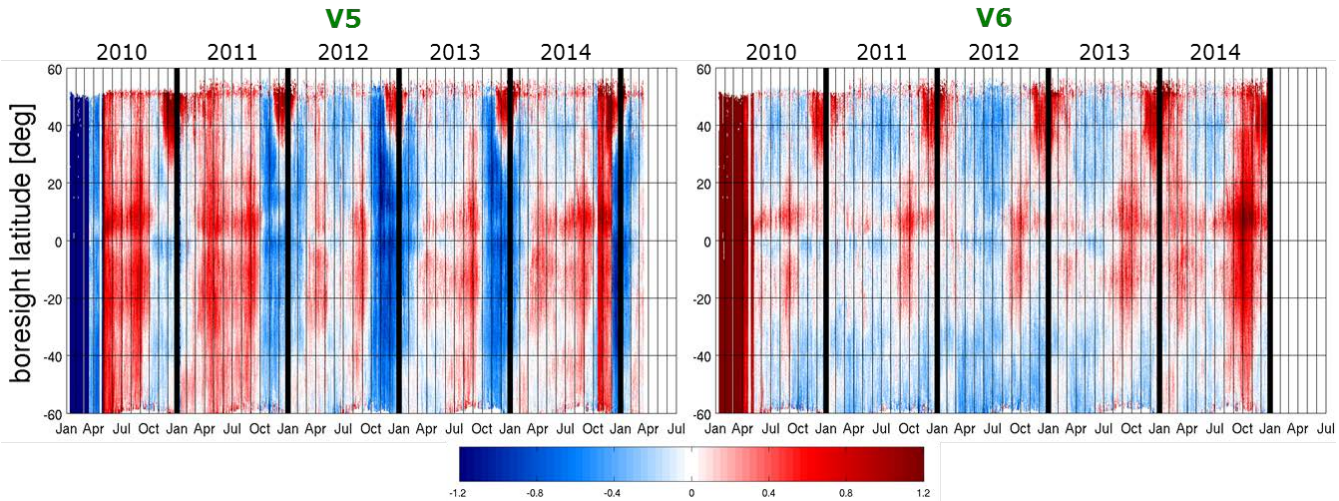

Figure 6: Latitude-Time **Hovmöller** plot of the descending pass Stokes-1/2deviation from an ocean forward model, averaged in the alias-free area, with V505 (left) and V620 (right) Level 1 processor versions. **Colour bar is given in Kelvin.**

3.1.5 Orbital Variations

The **top** right plot of Figure 7 shows the current difference between descending and ascending passes of the Stokes-1/2 parameter over the Pacific Ocean, averaged within the alias-free field of view. **The Stokes-1/2 parameters of each pass are first corrected for significant forward model contributions which range from tens of Kelvin (sea surface physical temperature and emissivity) to just a few Kelvin (reflected cold sky, galactic glint, direct and reflected Sun, atmospheric up and down welling). This correction is needed to separate geophysical from instrumental effects as much as possible.** The plot span in latitude and time, as well as the brightness temperature scale, are the same as those of Figure 6. The difference between **the two** passes, **shown in the bottom panel, is** within **0.8** K peak-to-peak, the maximum departure, of about +0.5 K, happening around October, **which is the period when the galactic glint is the strongest. There is evidence that such deviation in October is very likely related to a mis-modeling of the galactic glint.** It is worth mentioning that the descending minus ascending difference does not show any particular increase in 2014 as seen in the descending pass of Figure 6, meaning that both passes follow each other's variations also in 2014. **The top right panel of Figure 7 also shows a clear impact of the eclipse period in latitudes above 30° North.**

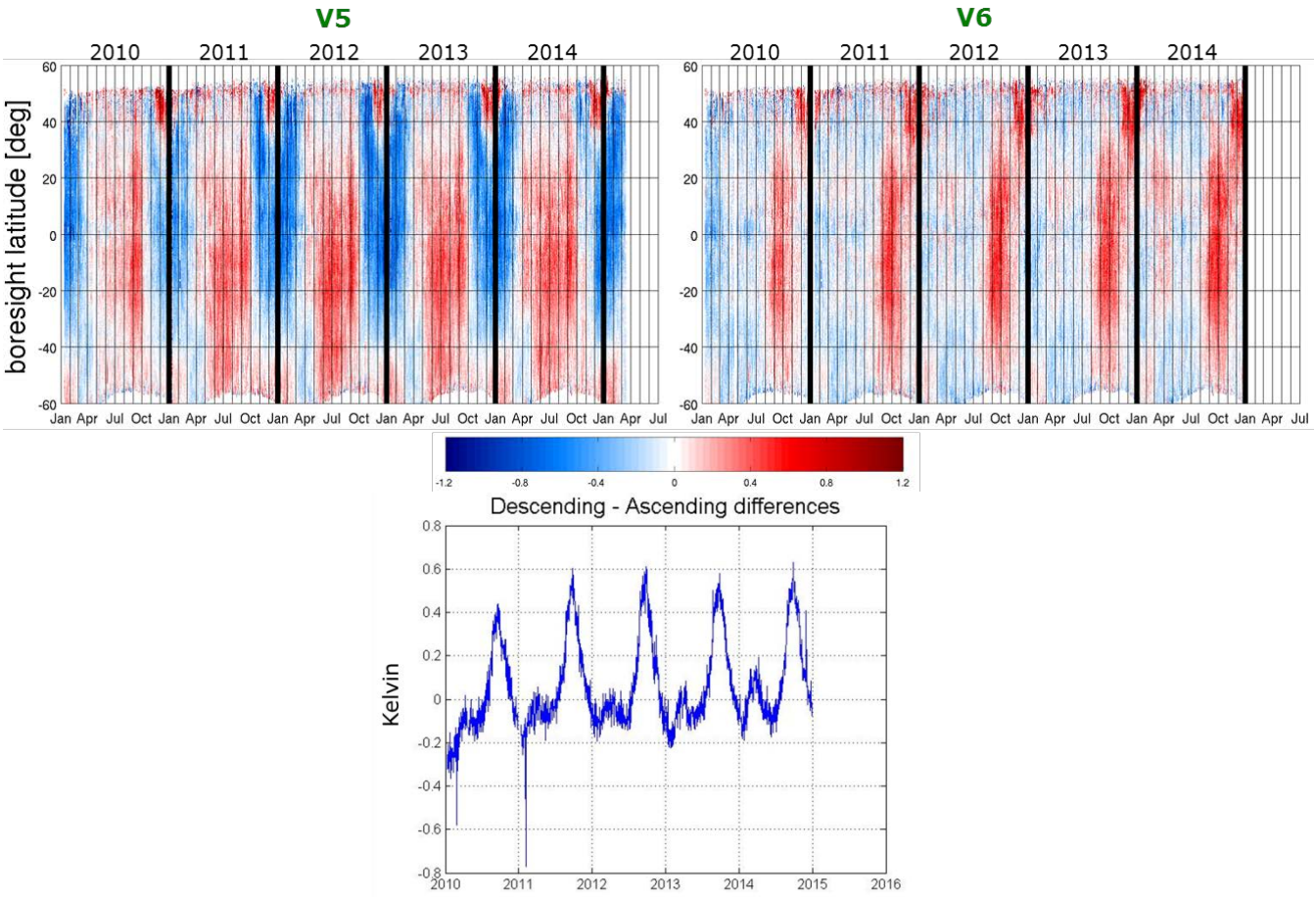

Figure 7: Descending-minus-Ascending pass Stokes-1/2 parameter over the Pacific Ocean, averaged in the alias-free area, with V505 (top left) and V620 (top right) Level 1 processor versions. **Colour bar is given in Kelvin. Same parameter averaged from 40° South to 5° North to avoid RFI and eclipse effects (bottom)**

3.2 Error Mitigation Techniques

This section presents a summary of the techniques which have been attempted to mitigate, with more or less success, the various error sources described in the previous section. The overall approach to mitigate any of the errors has been to first understand the mechanism causing them and to then build a new calibration or image reconstruction approach to reduce it. Empirical corrections have been avoided as much as possible, and when accepted, they have been applied just once for all 5 year data set. In this section the focus shall be in image reconstruction based solutions, leaving for a later section those improvements brought into the new in-orbit calibration plan.

3.2.1 Correction of Systematic Spatial Ripple

As explained earlier, given an antenna element spacing and a level of dissimilarity between the patterns of these, there is a minimum spatial ripple, the noise floor, which cannot be avoided. From a purely linear algebra point of view to the image reconstruction process, the noise floor can be understood with the help of Figure 8. A true brightness temperature distribution x_T in R^n space (with n being large) maps into y in the visibility domain in R^m (m also being large). However only a limited set of visibilities are actually measured, which in turn defines a fundamental hexagonal region in the physical space, smaller than the unity circle. Therefore only a visibility vector hat{y} projected onto the column space of the –assumed perfectly known– G matrix is available for inversion. Using the pseudo-inverse matrix of G, G^+, a least squares solution hat{x} is found, which belongs to the row space of the G matrix, at some unavoidable distance from the true brightness temperature distribution x_T, this distance defining the noise floor. The noise floor is therefore the component of the true brightness temperature vector in the direction of the null space of the G matrix, and is therefore proportional to the brightness temperature of the scene.

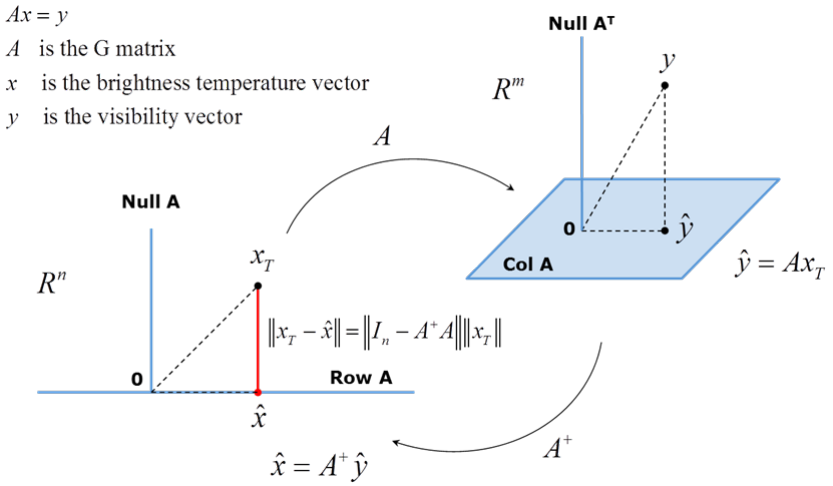

Figure 8: Noise floor definition

The following methods have been attempted, at Level-1 data processing, to mitigate the noise floor:

a) Amplitude Mask

This technique is based on assuming that the spatial ripple can be mitigated by the use of a multiplicative mask built over uniform targets like the Southern Pacific Ocean or Antarctica (Lin et al., 2011, 2012)(Torres et al., 2012).

b) Floor Error Mask (FEM)

A difference brightness temperature map is built between the measurements and what an ideal instrument would reconstruct. Such map is produced over a full year, and split into a scene dependent and a scene independent components. The latter is used to correct SMOS images for the scene independent spatial ripple (Anterrieu et al., 2015).

c) Pre-Distorted G-matrix (PDG)

Using the Binomial Inverse Theorem the G-matrix is pre-distorted a priori in order to reduce the error contribution due to antenna pattern differences (Díez-García et al., 2014).

d) Average Pattern Reconstruction (APR)

The visibilities are decomposed in two components, one corresponding to an instrument with identical antenna patterns (and receiver responses) and a residual. The residual is then removed from the visibilities and an image reconstruction using an instrument with identical antenna and receivers is performed.

e) Initial guess based techniques

These methods are based on the second result stated in the section devoted to the spatial ripple, i.e. that the scene content outside the alias free field of view has an impact on the recovered scene inside it. According to this result, it is desirable to reduce the brightness temperature content outside the alias free field of view, which can be achieved if a first guess of the scene is subtracted prior to the image reconstruction. The set of methods implementing this technique is referred to as “Gibbs” methods, as they try to reduce the contrast within the scene, hence the Gibbs ringing, and by extension, the spatial ripple (Camps et al., 2008)(Khazaal et al., 2009) (Corbella et al., 2014). There are different levels of Gibbs techniques with increased implementation complexity: Gibbs-0 assigns

a single value to the whole unity circle; Gibbs-1 differentiates between the sky and the Earth disk, giving a single value of brightness temperature to the whole Earth disk, and another one to the sky; Gibbs-2 introduces, in addition, a differentiation within the Earth disk between land and ocean masses, assigning a constant but different value to each part; an option of Gibbs-2 includes a Fresnel variation over incidence angle over the ocean, instead of using a single value; in Gibbs-3 the first guess is obtained from the long record of measured brightness temperatures as opposed to the use of models, as done in the previous cases.

The Gibbs-n techniques have been, among all, the most successful ones in reducing the spatial ripple. The success of the Gibbs-n techniques depends on the amplitude of any residual calibration errors. Nonetheless, because of the existence of the noise floor, it is unlikely that the current level of spatial ripple be significantly reduced in the future. The current Level-1 processor implements a Gibbs-1 technique, the remaining spatial ripple being removed at Level-2 through the Ocean Target Transformation (Gourion et al., 2013), to enable the retrieval of Sea Surface Salinity.

3.2.2 Correction of Sun and RFI Tails

Given the element spacing in SMOS, the aliases of the Sun are unavoidable. The mitigation of the side lobes joining the real Sun and its aliases, visible in the left panel of Figure 9 with peak amplitudes of the order of −18 dB, should be achievable through the application of a stronger apodization window in the spatial frequency domain than the nominal Blackman window (Camps, 1996) (Anterrieu et al., 2002). When a Circular window with much increased tapering than the nominal Blackman is applied to the spatial frequencies, the simulated response of the center panel should be obtained. Instead, the measurements, shown in the right panel, reveal that the side lobe level remains roughly at the same level (Torres et al., 2014). This puzzling result is a consequence, again, of the combination of the alias condition and the dissimilarities across the antenna patterns, as was the spatial ripple. In other words,

the noise floor sets a limit in the control that can be reached on the side lobes through windowing in the spatial frequency domain.

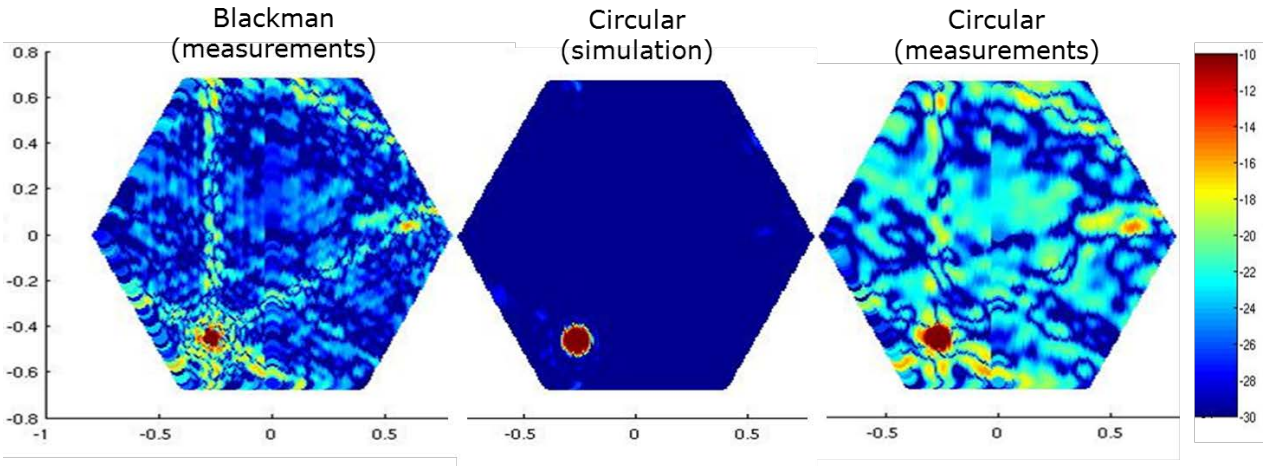

Figure 9: Measured Sun response with standard Blackman window (left), expected image with a stronger circular apodization window (center) and the corresponding measurements (right). **Colour scale gives the brightness temperature in logarithmic scale (dB-K).**

The following other techniques have been attempted to remove the Sun alias and its side lobes from the SMOS images:

a) Use of a measured Sun response

During one orbit of the 9th, 10th, 11th and 13th of January 2013, SMOS was pointed towards the galactic pole at a time when the Sun elevation was 21.3°, 17.1°, 10.1° and 21.6°, respectively, above the antenna plane. Four Sun responses were acquired over the uniform low cold sky background. These responses were later translated in position and scaled in amplitude, to correct for the Sun during measurements in nominal pointing. This method is still under research.

b) Use of an estimation of the Sun response

From an image contaminated by the Sun, the position and amplitude of the Sun are estimated, an artificial response is built based on them, and then subtracted from the original image (Camps et al., 2004). In this correction technique the most critical parameter is the accuracy in the localization of the Sun, which depends on the number of solar spots (Chiuderi Drago et al.

1977). An iterative process to estimate the position and brightness temperature of the Sun has shown promising results, but the increase in computational time is critical and is still under evaluation. A simpler method has been implemented in the Level-1 data processor of SMOS, with limited improvement, and has been complemented by flagging. Figure 10 shows an example of the Sun correction.

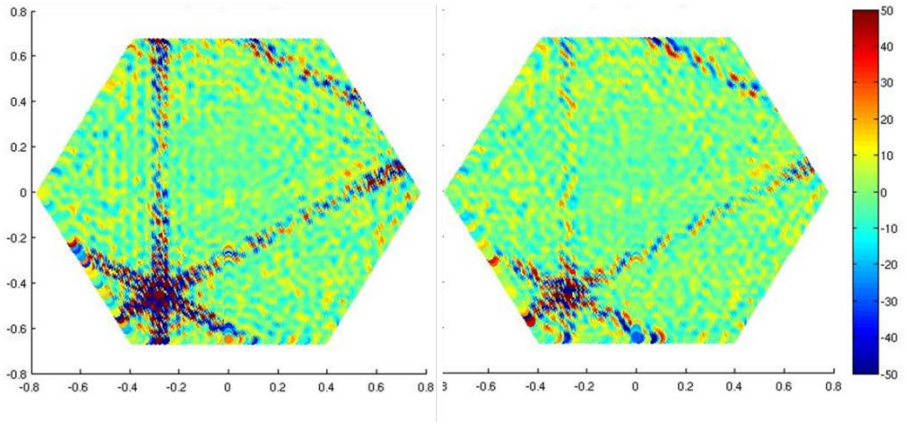

Figure 10: SMOS image of the Sun in cold sky pointing mode before (left) and after (right) Sun correction. Colour scale is in Kelvin.

In principle, the methods for the correction of the Sun alias and its tails can also be applied to remove RFI sources effects. However, the population of RFI sources is irregular, clustering in some regions of the Earth, with several interferors appearing at the same time inside the field of view of SMOS. In this situation a correction for the RFI sources of the type described for the Sun is difficult. Nonetheless, techniques to better detect, flag and correct for RFI sources keep being developed and assessed (Khazaal et al., **2014**). In parallel, a technique called the Nodal Sampling (González-Gambau et al., 2015) has been proposed to image RFI polluted areas and is under assessment, showing some promising results.

3.2.3 Correction of Land-Sea Contamination

During the investigation of the land-sea contamination error it has become clear that a mismatch between the amplitude of the visibility at the origin V(0,0) and the rest of the samples, V(k,j), generates this kind of degradation, as shown in the left plot of Figure 5. Empirically it has been proven that

affecting the correlator efficiency coefficients G_{kj} of the visibility samples V(k,j) outside the origin by a factor near 0.98 removes significantly the land-sea contamination. The right plot of Figure 5 shows the improvement when this correction is applied. The warm brightness temperature halos surrounding the continents have mostly disappeared. The possibility of correcting the correlation efficiency coefficients G_{kj} has been implemented in the latest version of the SMOS Level-1 processor (V700) and will be subject of validation before it is accepted to enter into operation.

It is worth mentioning that a parallel empirical correction of the land-sea contamination is being prepared at Level-2 based on a mask built with the 5 year long record of SMOS data (SMOS Level-2 Ocean Salinity Team, 2015).

3.2.4 Correction of Seasonal and Orbital Variations

The seasonal and orbital variations are observed in the right plots of Figures 6 and 7 respectively as warm anomalies around October and in the eclipse season every year. The current strategy to correct for these fluctuations is to simplify the calibration approach of the instrument as much as possible by using the All-LICEF mode (Torres et al., 2006) explained below and then attempt new corrections to mitigate them.

4 IN FLIGHT CALIBRATION PLAN

4.1 The Corbella Equation

The Corbella equation, introduced in 2003 (Corbella et al., 2004a), involves a fundamental modification to the formulation of interferometry, as used in radio-astronomy, that is necessary to describe the way an aperture synthesis radiometer of the type of MIRAS works. The calibration of SMOS is based on the Corbella equation, and hence, one of the first and most important tasks undertaken in the frame of the calibration of the instrument was its verification (Martín-Porqueras et al., 2010). Such exercise would ideally involve the imaging of two perfectly uniform black body targets

399 at two different physical temperatures. Since the Cold Sky near the galactic pole is the only reasonable
400 realization to such uniform target, the validation of the Corbella equation focused on the Cold Sky.
401 With the help of a simulator, two sets of visibility samples of the Cold Sky were produced using the
402 radio astronomy and the Corbella equations. Then, to improve contrast, the visibility samples at the
403 origin were set to zero, and a simple Fourier Transform was applied to provide the images of the
404 modified brightness temperature of the Cold Sky in each case. The image obtained using the radio
405 astronomy formulation is shown in the left panel of Figure 11, while the one resulting from the use of
406 the Corbella equation is in the right panel. These images were then compared to the one measured by
407 SMOS, shown in the center panel of Figure 11, which was generated in the same way, i.e. through a
408 Fourier Transform of the measured visibility samples setting the one at the origin to zero. The image
409 using the Corbella equation is very similar to that measured by SMOS, while the Cold Sky retrieved
410 with the radio astronomy equation does not capture any of the features present in the measurements.
411 This test validated the Corbella equation.
412

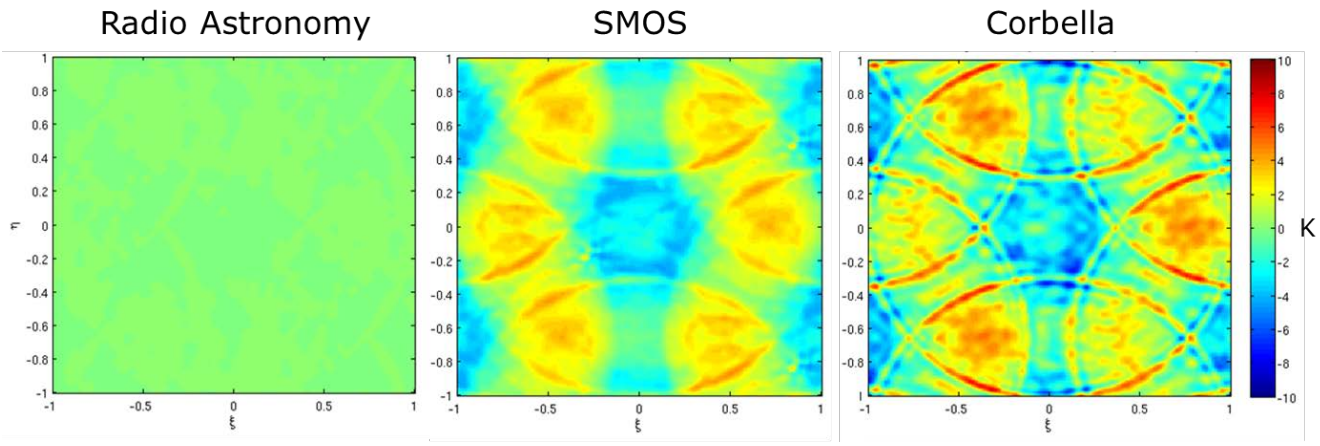

413
414 Figure 11: Expected modified brightness temperature of the Cold Sky using the radio astronomy (left)
415 and the Corbella (right) equation; center is the SMOS measurement (note: the visibility sample at the
416 origin has been set to zero to improve contrast)

417 **4.2 Routine In-orbit Calibration Plan**

418 The routine in-orbit calibration plan was established at the end of the Commissioning Phase, in May
419 2010. With the experience of the first year of the operational phase (Oliva et al., 2013), weekly Short
420 Calibrations while flying over Antarctica were added as from March 2011 to track the temporal

variation of the voltage offset of the receivers, leading to the calibration plan shown in Figure 12, which is the one currently used in SMOS.

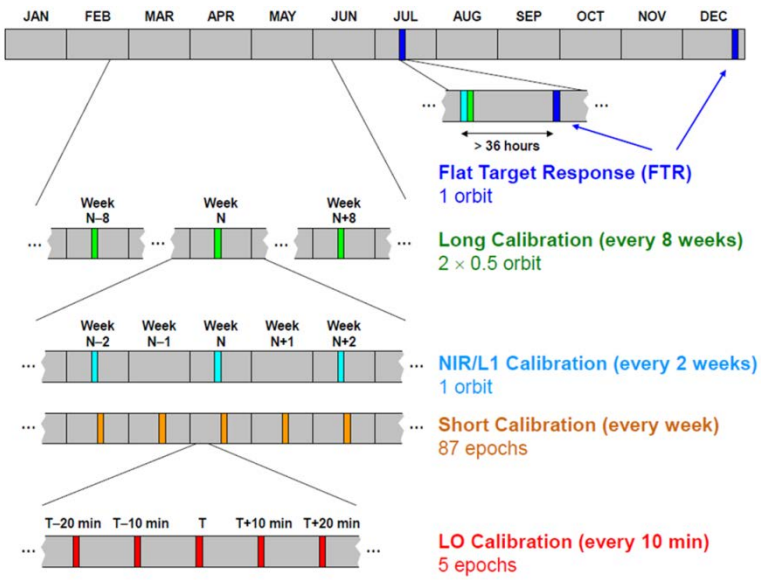

Figure 12: SMOS routine in-orbit calibration plan

4.3 In-flight Calibration Improvements

Two improvements have been made based on the in-flight experience over these 5 years: the "warm" external calibrations and the addition of an RFI check to validate the external calibrations.

4.3.1 Warm Calibrations

Detailed analysis of the external calibrations revealed that a few LICEF receivers of MIRAS exhibited small and smooth unexpected jumps in their PMS (Power Monitoring System) detector voltages. These jumps seemed to correlate well with the skin temperature of the antenna, happening more frequently for colder skin temperatures, and appeared to be reversible in the sense that, for warmer skin temperatures, the usual values were again obtained. To illustrate this, refer to the left panel in Figure 13, which spans one full orbit flown pointing zenith during the Commissioning Phase, **including the transitions from and to Earth pointing at the beginning and end of the plot, respectively**. The 3 cyan curves provide the skin temperature of the antenna measured by 3 thermistors (named Tp7). The black and green lines give, respectively, the elevation of the Sun over the antenna plane and its azimuth, in decadegrees as

read from the scale on the right. The Sun elevation is negative (the Sun is behind the antenna) except for a portion in the right half of the plot, where it reaches an elevation of about 30°. As soon as the Sun appears in front of the antenna the skin temperature (cyan lines) increases from near 0°C till some 20°C, to return back to just 1°C or 2°C as the Sun sets behind the antenna horizon. The dark blue and dark red crosses correspond to the detected voltages in the vertical and horizontal polarizations. The vertical polarization shows some fluctuations. The first anomaly appears towards the left of the plot when the physical temperature drops below some 10°C. At this moment the detected voltage jumps up a few millivolts, which is unexpected because as the instrument is pointed towards cold sky the detected voltage is expected to constantly decrease towards a minimum level. The anomalous higher value is maintained until the temperature rises again above some 12°C. Then several fluctuations happen centered around the maximum of temperature in the right half of the plot, showing a high degree of symmetry and correlation with the temperature evolution. The detected voltage attains a right value only in the center of these fluctuations, coinciding with the warmest temperature interval around the peak. It is plausible that these fluctuations could be related to a change in the electrical phase of some Teflon pieces of the antenna at some physical temperature range. Another example is given in the right panel of Figure 13, which corresponds to another of the affected receivers, this time during a typical external calibration manoeuvre: as the antenna cools down and its temperature reaches about 2°C, the detected voltages at the two polarizations experience jumps of 10 and 40 mV about. The purple line in the right panel is the estimated physical temperature at which the Teflon parts of the antenna could be. To avoid these voltage jumps, the external calibration manoeuvres are planned, since October 2014, **at a modified time to have** the Sun at some positive elevation angle over the antenna plane. The Sun illumination on the antenna keeps it warm, avoiding the skin temperature to fall too low and the PMS detector voltage fluctuations. The positive Sun elevation is however kept below a limit of 10° to ensure that its presence does not degrade the external calibration acquisitions. Careful checks were carried out to detect any effect from the direct signal of the Sun that could compromise the quality

of the external calibration. In addition the warm calibrations perform the external calibration with the antenna at a more similar temperature to the measurement mode, which is desirable, and reduce thermal excursion on the antenna, improving reliability. Warm calibrations can be planned any time along the year except around the equinoxes, when the Sun elevation is just too low, in which case, the usual cold calibrations are performed instead.

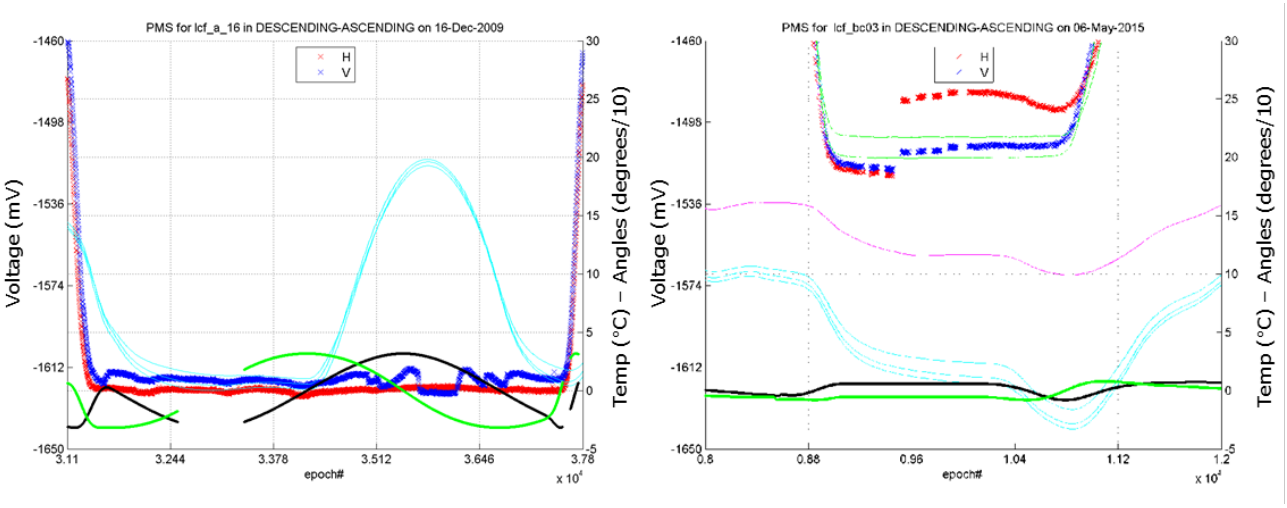

Figure 13: Example of PMS detector voltage fluctuations in a zenith pointing orbit (left) and during a typical external calibration (right) that led to the introduction of the external 'warm' calibrations

4.3.2 RFI Check in Validation of External Calibrations

External calibrations, where SMOS is pointed towards the Cold Sky, are executed only over the Pacific Ocean to avoid picking up signals from strong RFI transmitters on ground through the back lobes of the antennas. However, in one instance, an external calibration carried out 3 June 2015 in the North-Eastern Pacific Ocean, near Alaska, appeared contaminated by some ground interference. This caused some disturbance in the data production chain as the calibration file had been ingested before the problem was discovered. To avoid this, since then, every external calibration (these are performed once every 2 weeks) is manually checked for RFI degradation before being accepted for use in the Level-1 data processor. An automatic procedure is being built up to replace the manual check.

5 IN FLIGHT INSTRUMENT MONITORING

The values of some of the key instrument parameters which are monitored or calibrated in flight are presented next.

5.1 Physical Temperature

5.1.1 Skin Antenna Temperature

MIRAS carries a thermistor (labeled Tp7) inside the head of the central screw of the antenna of the 3 Noise Injection Radiometers whose readings are representative of the physical skin temperature of any of the antennas (Rubiales et al., 2015). This temperature is important because it affects the amount of noise emitted by the front end equivalent resistor. It also provides an indication on how different the thermal conditions of the antenna are between an external calibration and the nominal measurement mode.

The evolution of the temperature readings from the 3 Tp7 thermistors is shown in Figure 14. The skin temperature goes through its largest excursion (from about 6°C to 28°C) during **every** boreal winter solstice, when the Sun reaches maximum elevation above the antenna plane (around 31°) and is eclipsed by the Earth. There is a second period of large thermal excursion (from 8°C to 18°C approximately) around every boreal summer solstice where the Sun elevation reaches up to 15° elevation above the antenna horizon. During the equinoxes the temperature excursion is the smallest (between 5°C to 12°C) and the lowest skin temperatures are recorded, except for the external calibration events. The latter correspond to the individual spikes that drop below 0°C in Figure 14. The Tp7 temperatures went through an initial cooling transient, clearly observed during the first half of 2010, to then flatten out into a very small long term residual cooling trend.

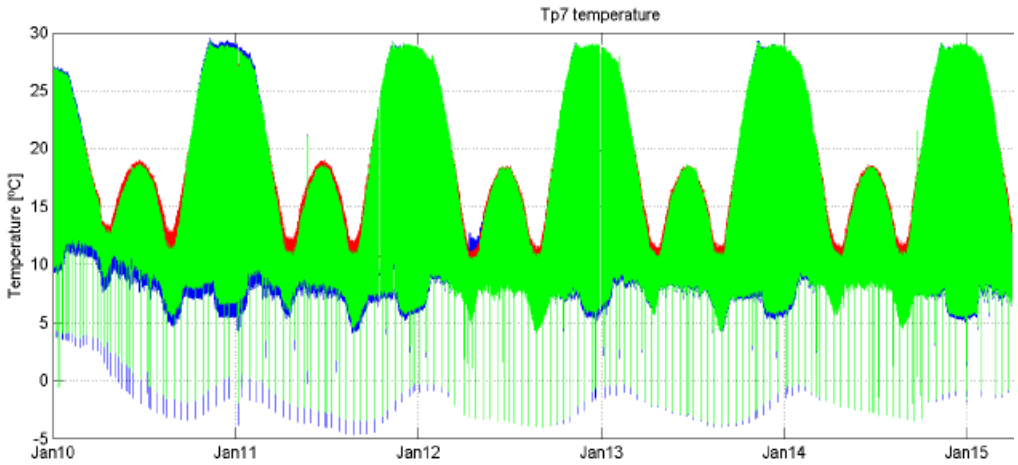

Figure 14: Evolution of the skin antenna temperature measured by the 3 Tp7 thermistors

5.1.2 Inner Receiver Temperature

Every one of the 72 LICEFF receivers of MIRAS has a thermistor (labelled Tp6) next to an internal matched load in the front-end electronics used as warm point in the amplitude calibration. This thermistor senses the inner temperature of the receiver. The average value of Tp6 across all LICEF receivers is shown in Figure 15. The physical temperature of the receivers is **seen** to be quite stable along the mission, centered around 22°C with a global peak to peak variation of about 1°C. As for Tp7, the Tp6 readings present larger excursions during the solstices, and narrower variation around the equinoxes, where its lowest values are attained.

5.2 Receiver Parameters

5.2.1 Antenna Losses

The antenna has two distinct loss components: one due to the radiating resonant cavity, and the other due to the intermediate layer circuit that combines the signal from the pair of probes of each polarization. The first component is tiny and difficult to measure on ground. It was estimated to be of about L1=0.05 dB, by calculations based on the geometry and materials of the antenna design. On the other hand, the losses of the intermediate layer circuit, of about L2=0.25 dB, was measured on ground. The total antenna losses are then expected to be around 0.30 dB. During the in orbit calibration, the

antenna loss are directly measured using the Cold Sky and the internal matched load (Corbella et al., 2012). The average value across all LICEF receivers for each polarization is shown in Figure 16. The in-flight measured antenna losses are about 0.17 dB larger than their pre-launch estimated value. It is worth noticing the rapid evolution exhibited during the first 6 months of the mission, as well as the seasonal fluctuations, the latter being partly driven by the PMS detector voltage fluctuations described earlier. The antenna losses present a different evolution after October 2014, reflecting the introduction of the warm external calibrations to avoid the mentioned PMS fluctuations.

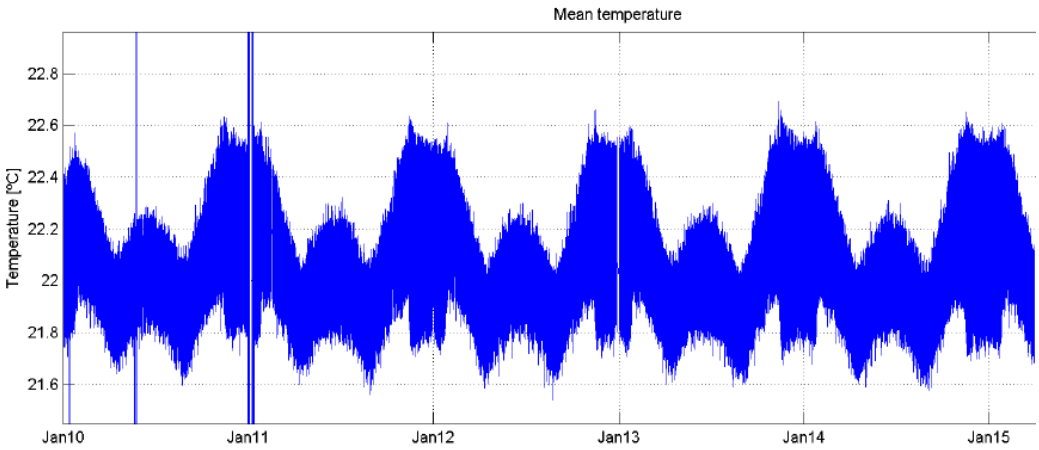

Figure 15: Average inner LICEF receiver temperature Tp6. **The spikes in early Jan'10, May'10 and Jan'11 are due to 3 anomalies occurred in the instrument.**

Figure 16: Evolution of the antenna losses as measured in flight

5.2.2 Receiver Detector Gains

The average detector gain across all LICEF receivers is presented in Figure 17 for each polarization. The absolute gain is shown in the left panel. Similar features to those found in the evolution of the

antenna losses are repeated here: an initial rapid transient followed by seasonal variations. In addition the receiver gains seem to be undergoing an exponential decay which, according to the relative gain variation shown in the right panel, has accumulated a total decrease of about 1.5%. **The reason for this decay is unknown, but could be caused by the overall thermal stabilization over mission life time.**

5.2.3 Receiver Detector Voltage Offets

The average voltage offset across all LICEF receivers is shown in Figure 18. The behavior is somewhat erratic, without any clear trend, with rapid fluctuations that led, in March 2011, to the introduction of weekly short calibrations as from March 2011 to track them. The voltage offset is therefore well followed with a weekly refresh rate and **calibrated** out.

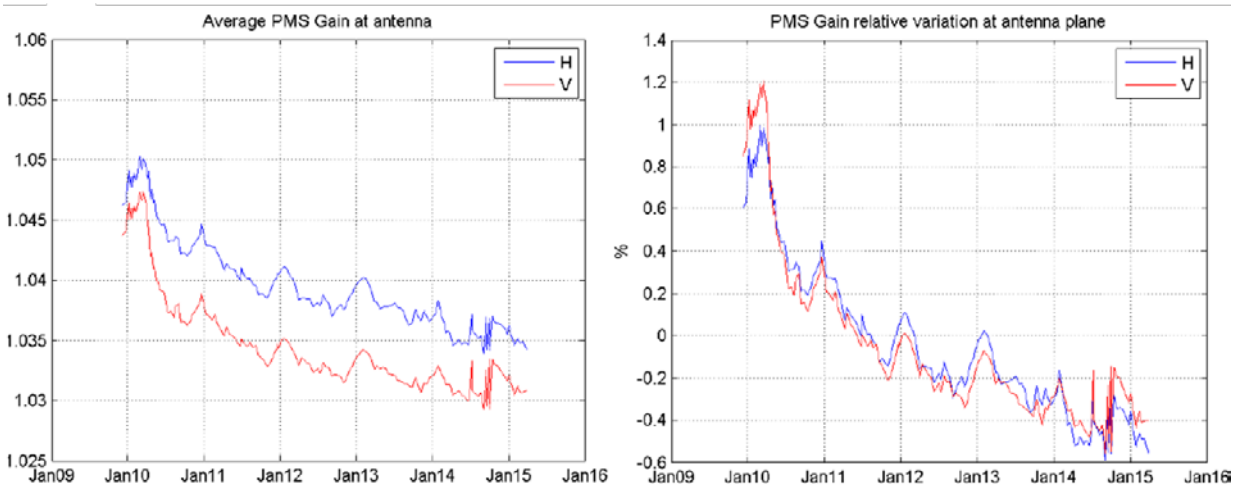

Figure 17: Evolution of the end-to-end average receiver gain in mV/K (left) and in percentage variation taking June 2011 as reference value (right)

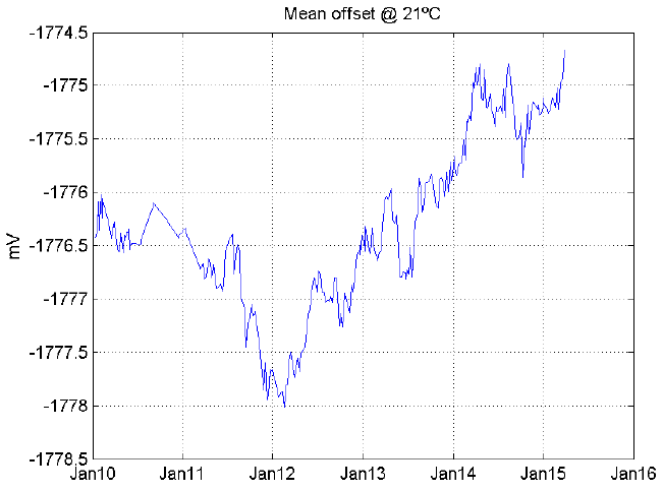

Figure 18: Evolution of the average detector offset voltage (in mV) across all LICEF receivers

5.3 Baseline Parameters

5.3.1 Relative Phase across Receivers

The relative phase across receivers is measured once every 10 minutes through the injection of a burst of correlated noise into all LICEF receivers. Phases between receivers sitting in different arm segments, hence fed by physically different local oscillators, present the strongest temporal variations. **In addition some of the 12 phase-lock-loop circuits available on board lose lock from time to time for reasons still unknown, but probably due to temperature (in total 9 unlocks per year, on average), generating phase jumps**. As an example, the phase between one receiver in the hub and other receiver in the first segment of one of the arms of MIRAS is shown by the blue line in the left panel of Figure 19. After correcting for any unlocks (blue spikes), the corrected phase in red is obtained. The fluctuations of the corrected phase are correlated with the physical temperature, which causes slight differential changes in the two local oscillators involved in the particular baseline.

On the other hand, the relative phase across receivers fed by the same local oscillator, i.e. sitting in the same arm segment, is rather stable, **and are not affected by the unlocks**. The right panel of Figure 19 brings the evolution of the relative phase across the 6 receivers of the third segment of one of the arms, shifted vertically only for presentation purposes. The peak to peak phase fluctuations are below 1° across the entire mission except for a few jumps that can be attributed to one specific receiver, probably caused by thermal expansion in one cable connection, but for which there is no proven explanation.

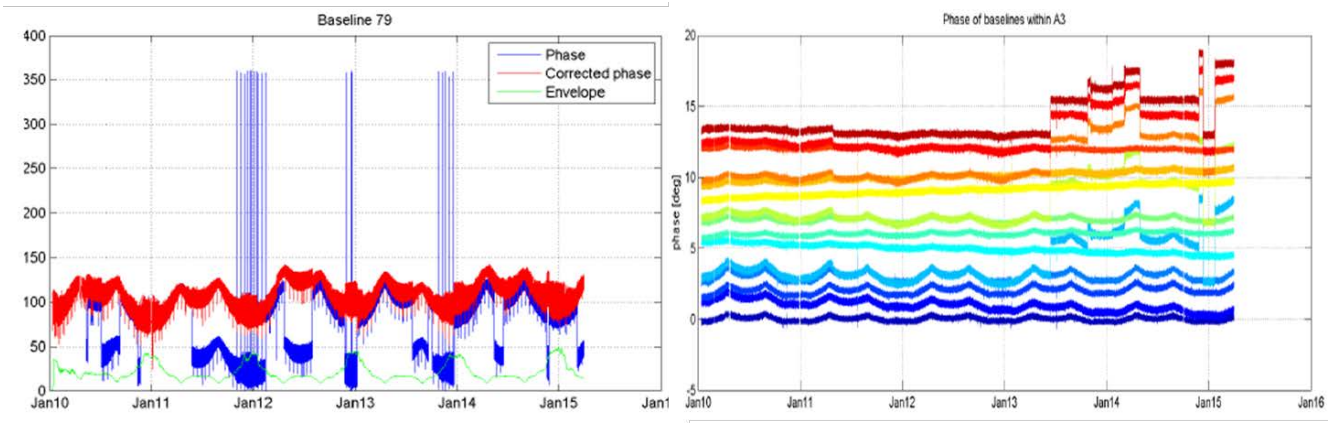

Figure 19: Relative phase between 2 LICEF receivers which do not share the same local oscillator (left) - spikes correspond to 360° wrappings - and across each of the 15 possible pairs from the set of 6 LICEF receivers of one arm segment connected to the same local oscillator (right)

5.3.2 Correlator Amplitude Coefficients

The average value of all the 2556 efficiency coefficients G_{kj} of the correlator for each baseline formed by receivers k and j is shown in Figure 20. **These G_{kj} coefficients represent the value of the so-called Fringe-Washing Function (FWF in short) at zero delay. They provide the correlation losses due to the on-board calibration network and the differences in the frequency responses of the receivers. The G_{kj} coefficients are used to denormalize the value of the raw correlations obtained from the 1-bit sampled signals. In theory the G_{kj} cannot be larger than 1, but because they are obtained through a combination of measurements of correlated noise injection from common Noise Sources (NS) and closure equations, some of them reach values slightly above 1.** The G_{kj} coefficients are very stable along the mission. The average of all G_{kj} is about 0.99, without any significant temporal trend.

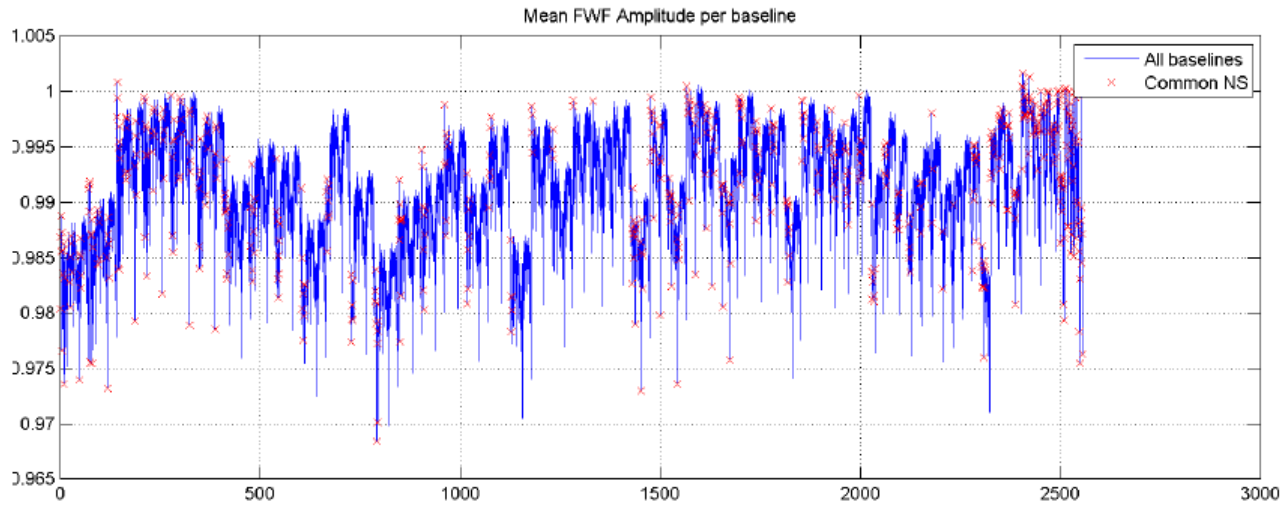

Figure 20: Average value of the G_{kj} correlator efficiency coefficients

5.4 Noise Injection Radiometer Parameters

The 3 Noise Injection Radiometers (NIR) embarked on SMOS are the reference radiometers of MIRAS (Colliander et al., 2007). They serve several purposes: (a) they measure the visibility sample at the origin; (b) they provide the reference antenna temperature to de-normalize the visibility samples obtained through 1-bit correlations; (c) they measure the amplitude of the noise diodes of the on-board Calibration System (Lemmetyinen et al., 2007); and (d) they are used as an additional receiver to generate visibility samples. A summary of their in orbit performance is presented next.

5.4.1 NIR Long and Short Term Stability

The NIR long term stability is illustrated in the left panel of Figure 21, which gives the error in each of the two polarizations against the Cold Sky for all external calibrations manoeuvres, performed once every 2 weeks, when a single calibration point, at the beginning of the Operational Phase (June 2010) is used. As it is shown, after the transient of the first 6 months of the mission (Kainulainen et al., 2010, 2012), the stability of the NIR units is remarkable: even when being calibrated only once in 4 years, the long term drift is only of about –0.1 K/year. The right panel of Figure 21 shows the short term stability of the NIR units by providing the Cold Sky error just before the NIR parameters are refreshed at every external calibration. The accumulated error over 2 weeks is within ±0.4 K. The bi-weekly external

637 calibrations remove completely **any long term drift**. **The annual behavior of the NIR error, that is**
638 **clearly seen in Figure 21 (left) is investigated a lot during the mission. Trials have been made to**
639 **relate the drift to internal instrument properties like physical temperatures, and to external**
640 **conditions, like Sun position or other components that contribute to the total antenna**
641 **temperature. Contributions of such external sources are reviewed e.g. in (Colliander, 2015), in**
642 **which forward geophysical model simulations were used to simulate NIR antenna temperature**
643 **measurements**.

644 **The observed 0.13 K standard deviation error of the sky measurements in Figure 21 scales down**
645 **to about 0.1 K error in measurement pointing mode (Kainulainen et al, 2012), a smaller error**
646 **than the 0.2 K radiometric resolution of the NIR units, and thus, not affecting the retrieval of the**
647 **geophysical parameters.**

648

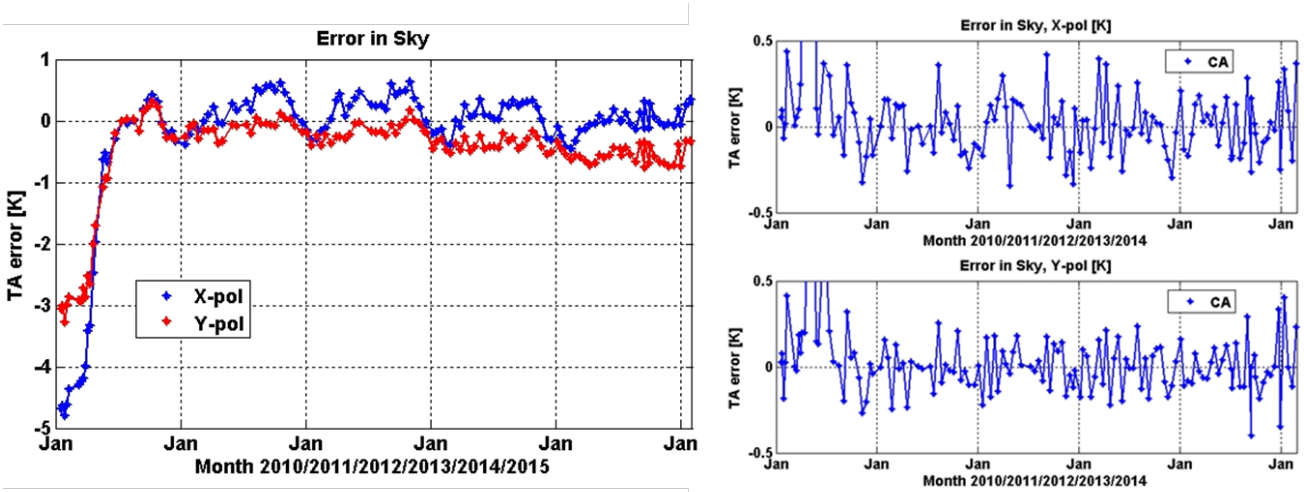

649
650 Figure 21: **NIR-CA** stability when calibrated only once (left) or every 2 weeks (right)
651
652 **5.4.2 Noise Injection Temperatures**
653
654 NIR uses some internal noise diodes to operate. The stability of these diodes and their injection circuits
655 are critical to establish the performance of the NIR units and the whole MIRAS instrument. Two levels
656 of noise injection temperatures are used, a low one T_{na} to measure the antenna temperature, and a high
657 one, T_{nr} to measure the diodes of the on-board Calibration System. Figure 22 shows the 5 year
658 evolution of T_{na} and T_{nr} in the left and right panels respectively, for the horizontal polarization (similar

results are obtained in vertical polarization). Besides the initial transient, the variations over 5 years are within 0.2% peak to peak for the most stable unit, NIR-CA.

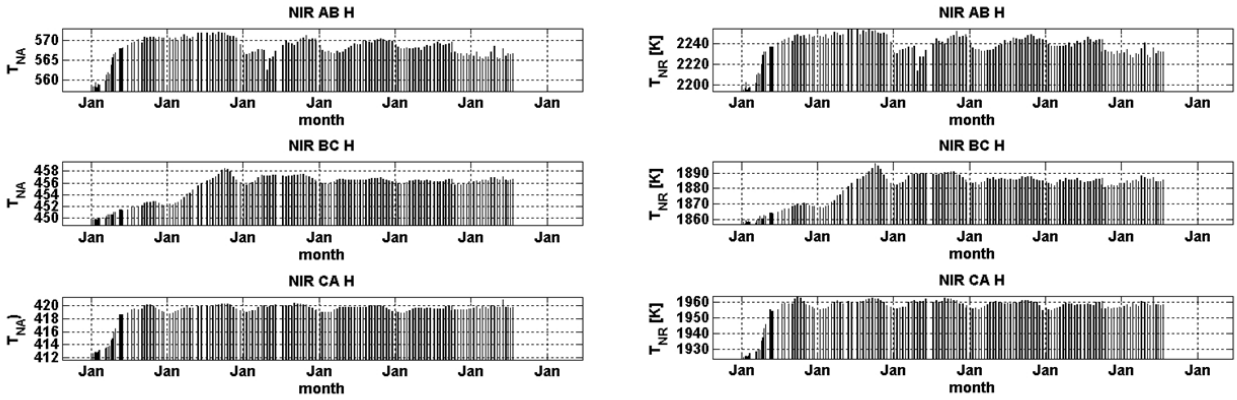

Figure 22: Temporal evolution of the noise injection temperatures of the NIR units

6 SMOS LEVEL-1 DATA PROCESSOR PERFORMANCE

Figure 23 shows the evolution of the SMOS Level-1 data processor that transforms the raw visibility samples into calibrated brightness temperature records. The first version used during the Commissioning Phase (November 2009 till May 2010) was V324 while the first processor supporting the Operational Phase was V344. During 2011 version V500 was deployed and a full reprocessing of the mission data set between January 2010 till October 2011 was carried out with a slightly modified version V505. A new version V600 was ready by end of 2012, which, after further enhancements, became V620 by early 2014. A second full mission reprocessing of the data between January 2010 and May 2015 took place using V620, version which was deployed in early 2015. This section will focus on the improvements brought in by V620, used in the second reprocessing, with respect to the earlier V505 of the first reprocessing, as well as in the performance assessment of the new processor version.

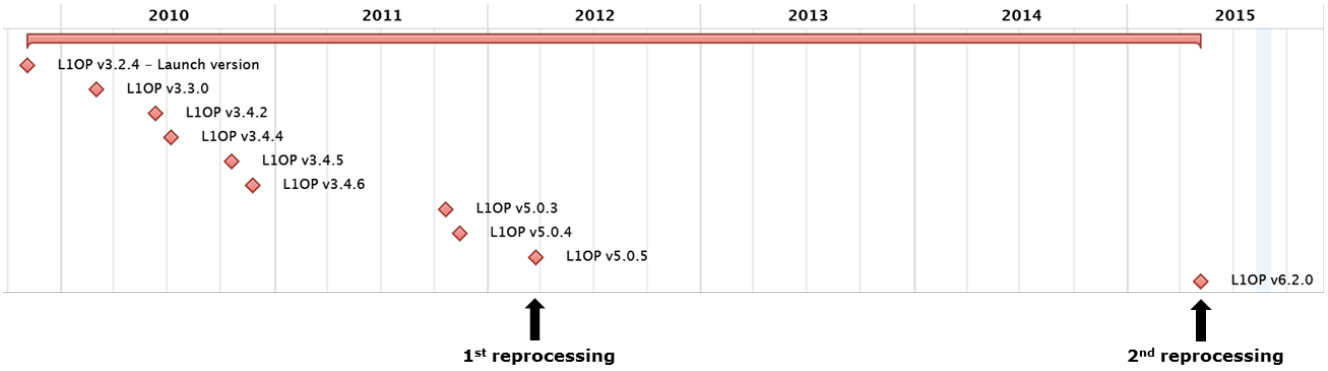

Figure 23: SMOS Level-1 data processor evolution

6.1 Enhancements in Level-1 Processor Version V620 over V505

6.1.1 Fully Polarimetric Operation

The equation below gives the matrix relation between the brightness temperature and the visibility vectors through the G observation matrix (Martín-Neira et al., 2002) (Corbella et al., 2004b):

$$\begin{bmatrix} \Delta V_{kj}^{HH} \\ \Delta V_{kj}^{VV} \\ \Delta V_{kj}^{HV} \end{bmatrix} = \begin{bmatrix} G_{T_{HH}}^{HH} & G_{T_{VV}}^{HH} & G_{T_{HV}}^{HH} \\ G_{T_{HH}}^{VV} & G_{T_{VV}}^{VV} & G_{T_{HV}}^{VV} \\ G_{T_{HH}}^{HV} & G_{T_{VV}}^{HV} & G_{T_{HV}}^{HV} \end{bmatrix} \times \begin{bmatrix} \Delta T_B^{HH}(\xi,\eta) \\ \Delta T_B^{VV}(\xi,\eta) \\ \Delta T_B^{HV}(\xi,\eta) \end{bmatrix}$$

The elements along the main diagonal of the G matrix involve co-polar antenna patterns. The elements outside the main diagonal include one or two cross-polar patterns. V505 was built using only co-polar patterns, that is, the G matrix was block-diagonal. The new version V620 makes use of the cross-polar patterns, which were measured on ground, and hence, implements a fully populated G matrix with all the blocks shown above. The first attempts to use the cross polar patterns were not successful though, because there was a sign inconsistency between the ground measurements and the Level-1 data processor. Once this issue was identified and solved, the expected performance improvement was achieved (Torres et al., 2015). The G matrix is used inside the Level-1 processor in the forward modelling as well as in the inverse process of image reconstruction (Khazaal et al., 2015). V620 is the first fully polarimetric SMOS Level-1 data processor. **Among all enhancements, this one providing fully polarized data is perhaps the most significant one. In fact, this is the first time that fully polarized interferometric images from space are processed.**

6.1.2 Use of the Relative Phase between Polarizations Measured on Ground

During the Image Validation Test (IVT) of MIRAS that was carried out on ground before launch, a set of 4 probes was placed in the ceiling of the Maxwell Electromagnetic Compatibility chamber of ESTEC to measure the relative phase between all LICEF receivers (Corbella et al., 2009). The instrument was operated in both dual and full polarization. For version V505 of the Level-1 processor, 2 separate sets of relative phases were retrieved from the IVT test: one with the relative phases for the horizontal polarization and another one for the vertical polarization. When preparing the next version, V620, of the processor, it became clear that the two sets of relative phases could have an offset between them which had to be corrected. Such phase bias across the two polarizations was in fact causing distortions in the Stokes-3 and, most clearly, Stokes-4 parameters. Therefore, the IVT data set was re-analyzed to determine the missing phase offset between the two polarizations, which was found to be of –6.8°. This value was verified using Stokes-4 images over the ocean: as shown in Figure 24, the error (sigma displayed in the lower left corner) was indeed minimized for a phase offset close to the retrieved one. All phases corresponding to vertical polarization were then reduced by that amount in version V620 of the processor.

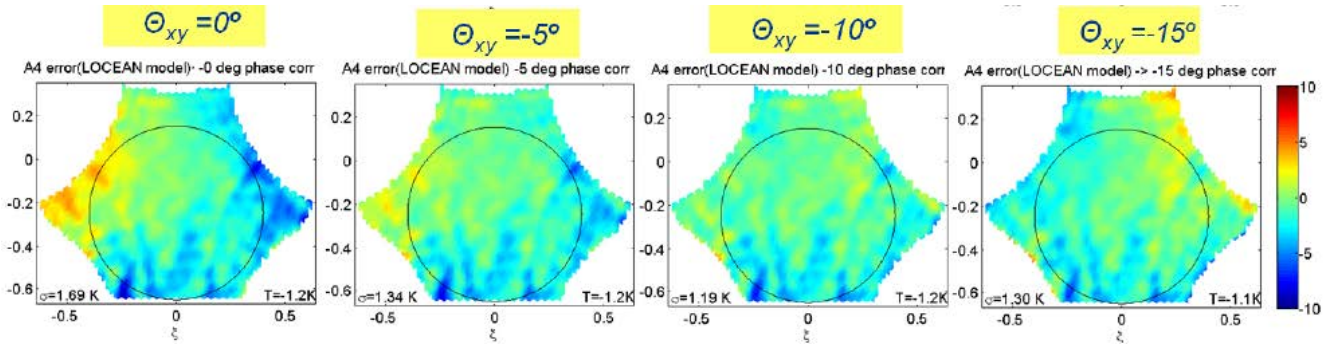

Figure 24: Validation of the relative phase between polarizations using Stokes-4 over ocean.

6.1.3 Use of Average Antenna Patterns across 3 Frequencies Measured on Ground

The antenna patterns of all and every element of MIRAS embedded in the array were carefully measured in an antenna test range. The measurements were performed at the center frequency, 1413.5 MHz, as well as at the band edges, 1404 and 1423 MHz. In version V505 of the Level-1 processor only

the patterns at the center frequency were used. In version V620, the average antenna pattern across the 3 measured frequencies is used, which reduces slightly the spatial ripple, as shown in the left lower corner of each panel of Figure 25.

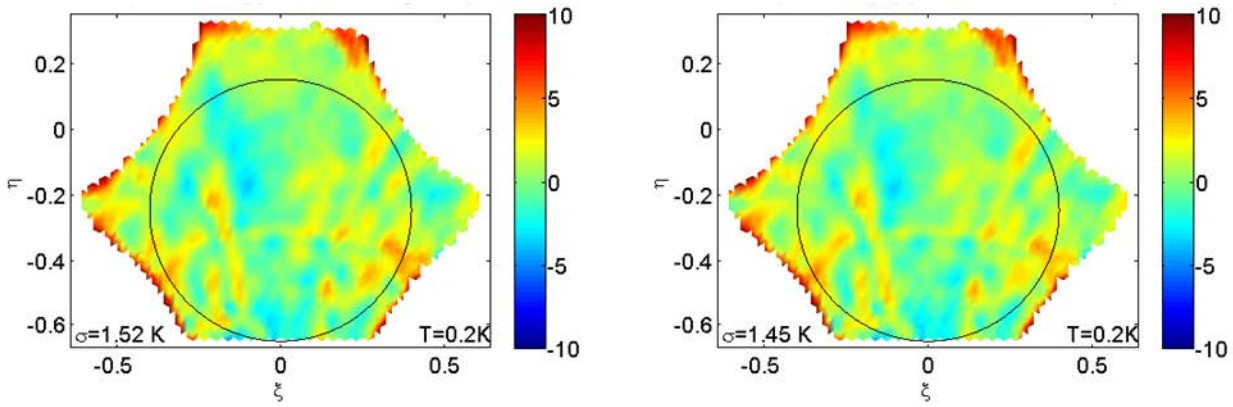

Figure 25: Deviation images from an ocean model in X-polarization using 1 pattern (left) or the average of the 3 measured patterns on ground (right) –similar results were obtained in Y-polarization–.

6.1.4 Replacement of Antenna Pattern of Hinge Elements by their Neighbour's

Analyzing in detail the measured antenna patterns, it was noticed that those corresponding to elements next to one of the hinges of the deployed arms (upper left panel of Figure 26), presented some ripples which the elements in the center of the arm segments did not exhibit (upper center panel). Some research led to the conclusion that these ripples were caused by travelling waves between the arm and the supporting structure that was used to hold it during the measurements, as shown in the lower left panel of Figure 26, which would leak out through the next hinge and segment contour causing a typical interference pattern. Since the instrument in flight configuration does not have any supporting structure in the back, the real patterns of the hinge elements should be free of fringes and similar to those of the central elements in each arm segment. For this reason, in the Level-1 processor version V620, the antenna patterns of the hinge elements was replaced by that of its inner neighbours, which reduces slightly the spatial ripple of the images, as illustrated in the right panel of Figure 26, to be compared to the left panel of Figure 25.

6.1.5 Use of Only the Most Stable NIR Unit

From Figure 22, it is seen that the NIR-CA unit (bottom panels) is the most stable of the 3 Noise Injection Radiometers of MIRAS. To assure the best temporal stability, it was decided to use, in V620, only the antenna temperature measured by NIR-CA, and not those from **NIR-AB** and NIR-BC, for the visibility sample at the origin V(0,0). All 3 NIR units are still employed in the measurements of other visibility samples outside the origin as well as in the measurement of the noise diodes of the on-board Calibration System.

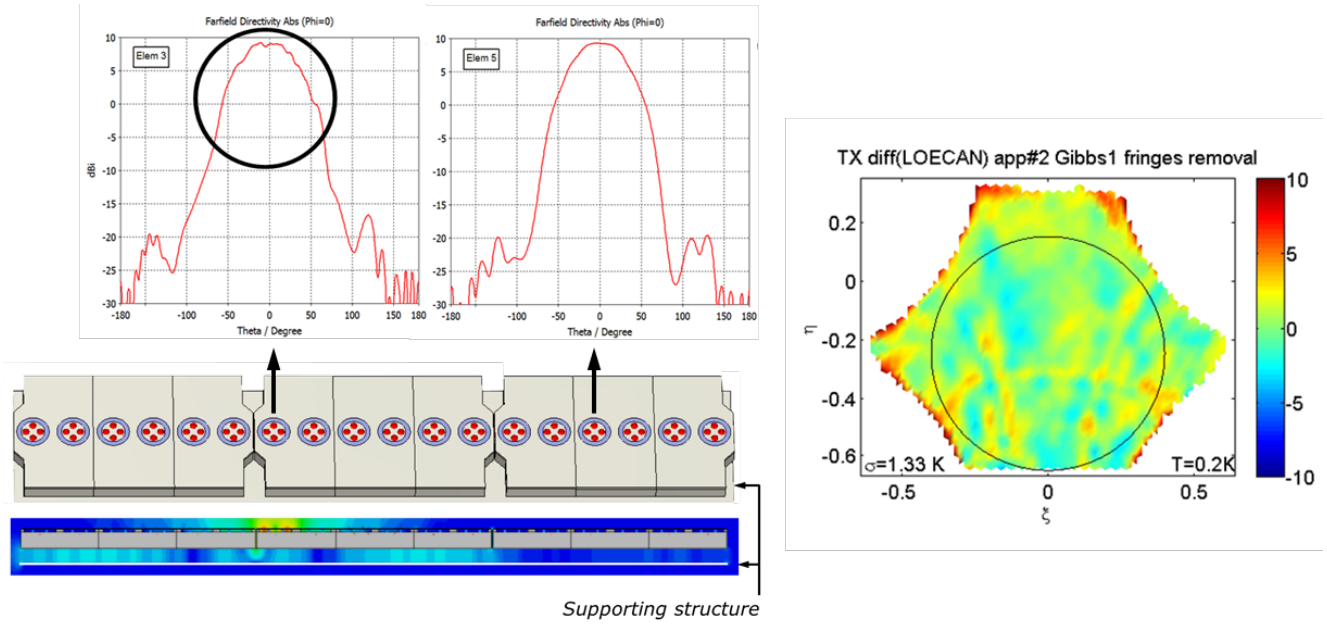

Figure 26: Antenna patterns of elements next to a hinge (top left) and away from it (top center); electromagnetic simulation showing leakage between arm and back supporting structure (left bottom); image obtained by replacing hinge patterns by their neighbour's (right).

6.1.6 Use of In-Orbit Antenna Loss

As mentioned earlier, antenna losses L1+L2 could not be accurately measured on ground due to set up uncertainties, and instead, were characterized in orbit, for V620 of the Level-1 processor, thanks to the more favourable external calibration manoeuvres (refer to Figure 16). The final estimation of the antenna loss was carried out after removing those instances with detector voltage fluctuations as the examples in Figure 13. Once the total loss had been measured, a second step, critical for the temporal stability, was performed, that of determining the L1 and L2 separately for the Noise Injection Radiometers. As the external calibration could only provide the ensemble loss, the split into its two

contributions was done by minimizing the orbital variations, **taking as metrics the descending minus ascending deviations** over the ocean with respect to a forward model. Such exercise resulted in a minimum of orbital variation for L1=0.15 dB as illustrated in Figure 27, the remaining of the total loss measured in orbit being assigned to L2. The values used in V620 for the L2 antenna loss of each receiver and polarization are constant (do not change over time) and equal to their average value obtained across all external calibrations, using the optimized L1=0.15 dB. **This procedure to split the antenna losses in its two contributors L1 and L2 was based on the much stronger relationship of L1 with orbital variations than L2, L1 being tightly influenced by the skin temperature of the antenna.**

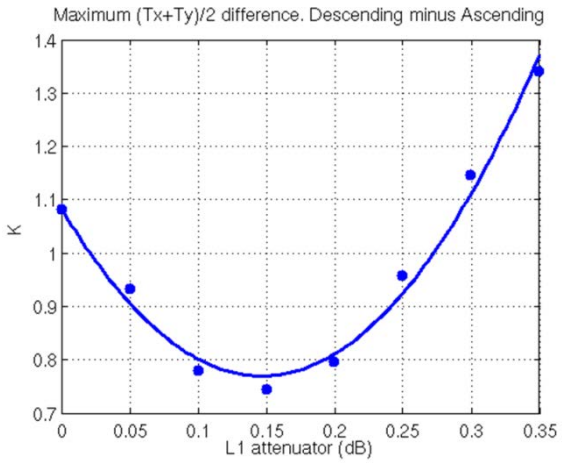

Figure 27: Split of NIR antenna losses achieved by minimizing the descending minus ascending pass difference of the deviations of the first Stokes parameter (divided by 2) from a model of the brightness temperature of the ocean (in Kelvin)

6.1.7 Improved Gibbs-1 Image Reconstruction

In addition to being fully polarimetric, as commented earlier, the image reconstruction of V620, depicted in Figure 28, brings two other main improvements over V505. The first one is the implementation of the whole processing on hexagonal grids, as opposed to rectangular ones, to avoid interpolation errors. The second consists of a new Gibbs-1 'model approach' by which the image reconstruction is performed over residual visibilities resulting from subtracting the estimated contribution of the Corbella term, the sky and the Earth, from the measured visibilities.

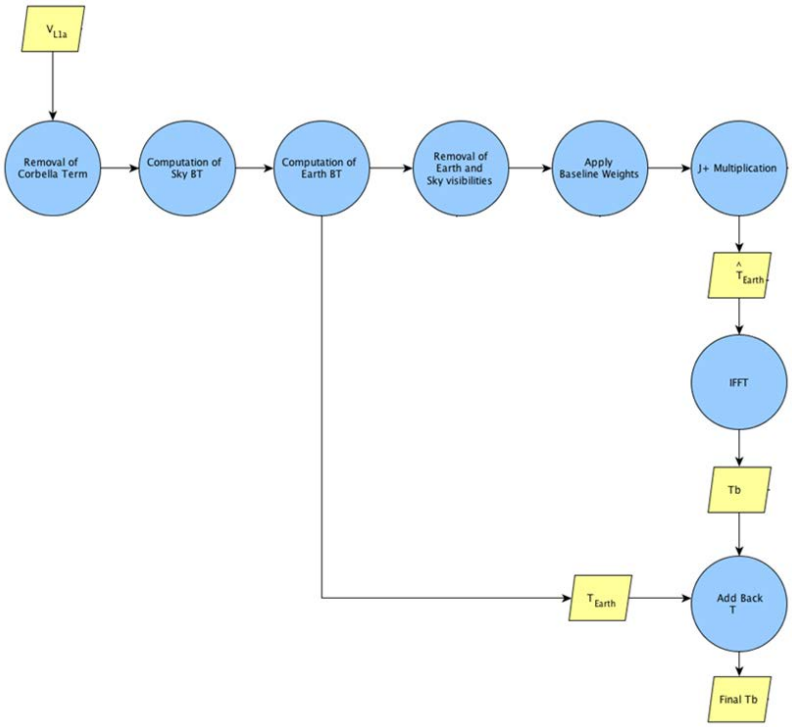

Figure 28: Improved Gibbs-1 model approach for image reconstruction as implemented in V620.

6.1.8 Improved Removal and Flagging of Sun and RFI sources

Since version V505, the algorithm for the Sun removal has been continually improved. In V620 the Sun brightness temperature is estimated through a 4-point **spatial** interpolation instead of taking the single closest neighbour point, this allowing a much finer positioning of the energy and thus, a reduction of the Sun tails. Several enhancements were also done to the flagging of the pixels affected by the Sun brightness temperature, in particular, the dynamic adjustment of the width of the tails of the real Sun and its aliases for every snapshot, and the correct flagging of all tails (one of the tails was not properly flagged in the previous version), as shown in Figure 29. As for the flagging and treatment of RFI sources and their impact, the improvements are reported in (Oliva et al., in press) (Khazaal et al., 2014) (Daganzo-Eusebio et al., 2013).

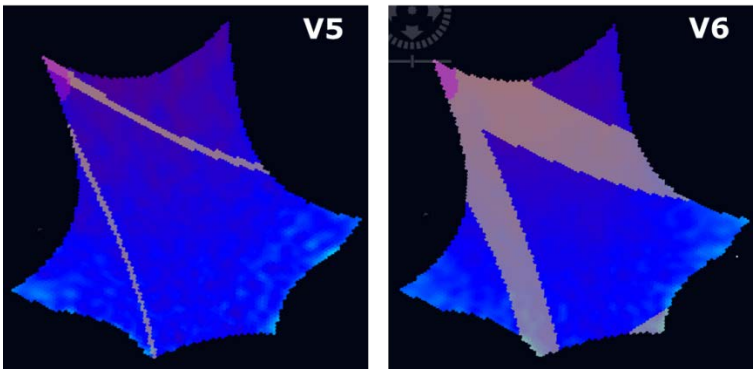

Figure 29: SMOS extended alias-free field of view showing, in grey, the pixels which are flagged due to the Sun tails (real Sun is on the right, with 2 alias on left top and left bottom). The width of the tails with flagged pixels has been increased with the improved Sun tails dynamic flagging of V620, and all tails are now flagged (note the lower right corner tail in V6).

6.2 Performance of Level-1 Processor Version V620

This section is devoted to present the performance of the currently operational version of the Level-1 processor, V620, in comparison with the earlier version V505. The performance has been assessed over the entire data set of the two reprocessing campaigns, one with each processor version. The quantification of the performance has been carried out following some defined metrics, as depicted in Figure 30, comprising: calibration parameters, temporal stability (orbital, seasonal and yearly) of both the antenna and the brightness temperatures, systematic spatial errors in the images (bias and ripple), Sun correction, land-sea contamination and random noise. The Cold Sky, the Pacific Ocean and Antarctica are the targets where the metrics have been evaluated, **by comparing observations to a surveyed map of the sky, a radiative transfer model of the ocean (Ocean Target Transformation or OTT) or simply their average value over Antarctica (Ice Target Transformation or ITT) respectively.**

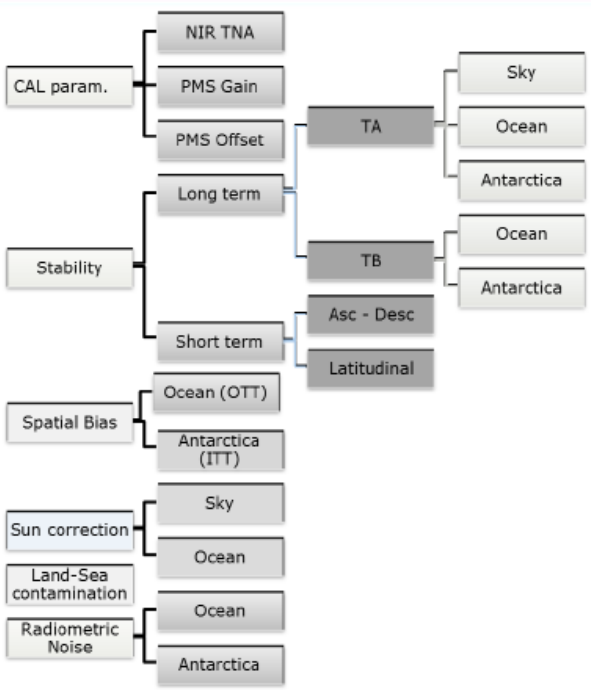

Figure 30: Overview of the metrics used to evaluated the performance of the Level-1 processor.

6.2.1 Removed Negative Slope at High Elevation Angles

V505 suffered from a negative slope in the dependence of the brightness temperature with elevation angle, in a way that measurements at low incidence were too cold when compared against modeled values. This is illustrated in the left panel of Figure 31 which shows the brightness temperature measured by SMOS, in horizontal and vertical polarizations, as a function of incidence angle over Dome-C station in Antarctica (Macelloni et al., 2013). As reference, the red dashed line represents a model, the diamonds are Aquarius observations and the solid circles ground measurements. Besides the discrepancy at high incidence angles which is expected due to the unavoidable sky contamination in the ground observations **(through the part of the main lobe above the ice horizon)**, the SMOS brightness temperatures are clearly colder than the model towards 0° incidence. The enhancements implemented in V620 described earlier **(in particular in Section 6.1.7)** resulted in a substantial reduction of such cold trend at low incidence, as can be seen in the right panel of Figure 31. It is also worth noting that, for V620, the ripples along incidence angle are smaller and the match with Aquarius and Dome-C ground radiometer is better.

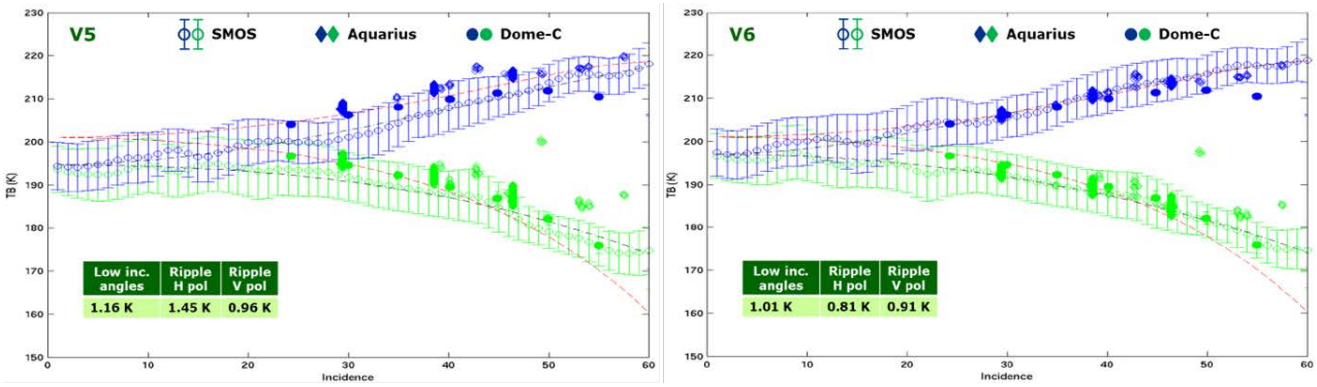

Figure 31: Performance of V505 (left) and V620 (right) with incidence angle over Antarctica.

6.2.2 Lower Spatial Ripple

Although there is a limit to how much the spatial ripple can be removed as explained before, Figure 32 shows that V620 achieves about 0.2 K lower spatial ripple in both polarizations than V505**, thanks to the improvements in Sections 6.1.1 through 6.1.4 and 6.1.7.** The root mean square spatial ripple of V620 over most of the Extended Alias-Free Field of View is therefore of about 1.5 and 2.0 K for X and Y polarizations respectively, evaluated over the ocean. It has to be noted that the bias of V620 is warmer than that of V505, overshooting almost 1 K in X polarization above the forward ocean model.

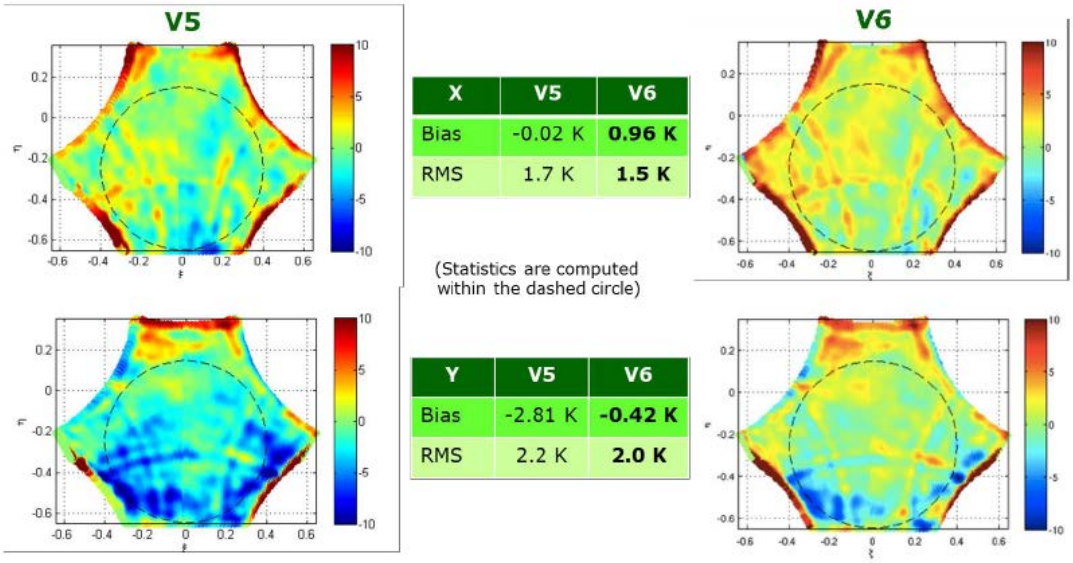

Figure 32: Spatial ripple and bias of V505 (left) and V620 (right) over Ocean **(colour scale in Kelvin)**

6.2.3 Improved Stokes-3 and Stokes-4 Parameters

The fully polarimetry operation of V620 including the cross-polar patterns with corrected sign convention **(Section 6.1.1)** and relative phase between polarizations **(Section 6.1.2)** yield significant improvements in the Stokes-3 and Stokes-4 parameters (Lin et al., 2013). This is clearly shown in Figure 33, where more uniform residuals against the ocean model are obtained with V620 (right column) than with V505 (left column). The cleaner polarimetric brightness temperatures provided by V620 allows accurate estimation of the ionospheric total electron content and the Faraday rotation angle directly from SMOS observations (Corbella et al., 2015).

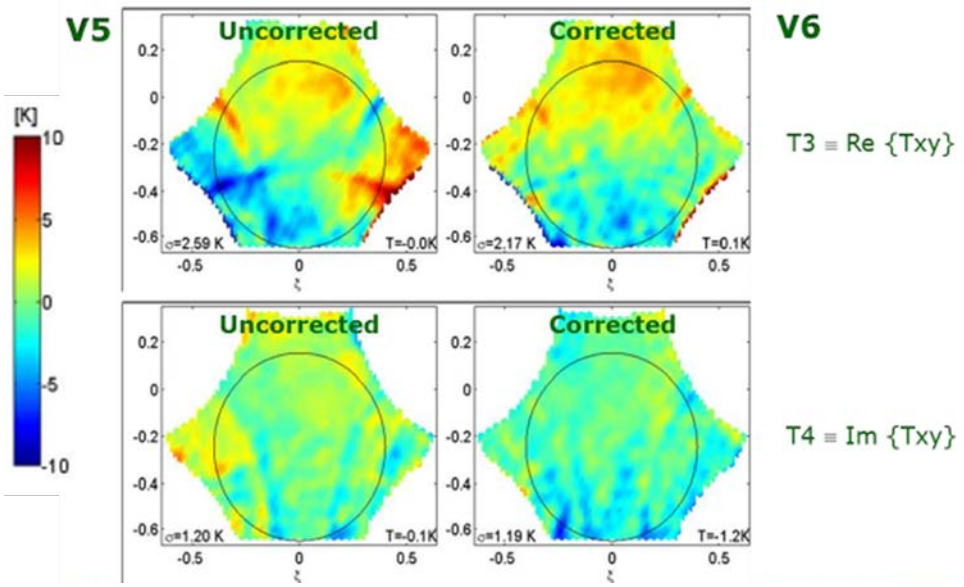

Figure 33: Residual Stokes-3 (top) and Stokes-r4 (bottom) of V505 (left) and V620 (right) over Ocean **(colour scale in Kelvin)**

6.2.4 Removed Latitudinal Drift

The red line in Figure 34 shows the deviation of the Stokes-1/2 parameter (average of the vertical and horizontal brightness temperatures) against a forward model along a strip of the Pacific Ocean from 50° South to 20° North, for version V620. **The plot is for one orbit, but the general behaviour is systematic, with some seasonal variations as shown in the Hövmoller plot in the right panel of Figures 6.** Besides some variations **on each side** of the equator which can be related to geophysical signals **(unmodeled rain and surface roughness effects)**, there is no tendency with latitude as expected**, thanks mainly to the improvement in Section 6.1.6**. This is an important improvement

881 over V505 processor, for which the Stokes-1/2 parameter, shown by a blue line on the same figure, did
882 have a significant slope over latitude.

883

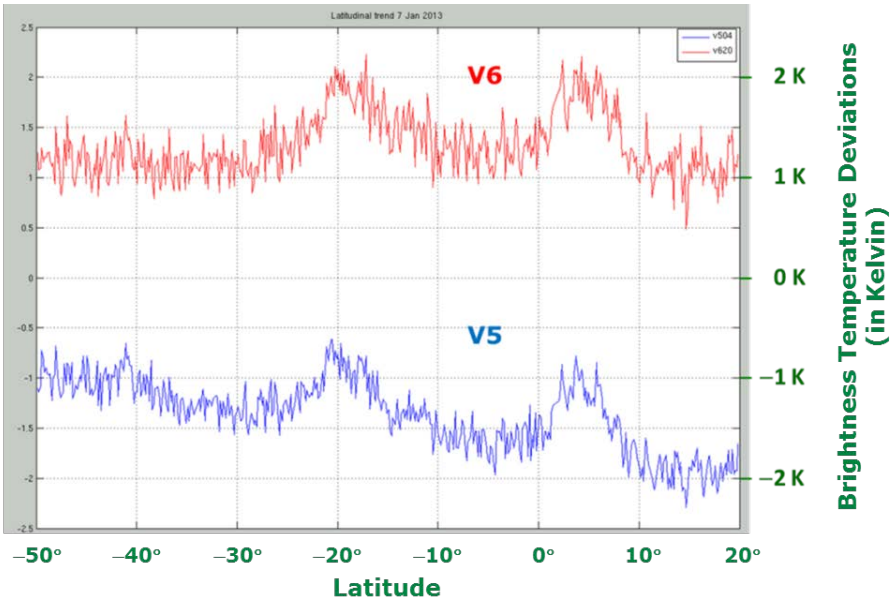

884
885
886 **Figure 34: Latitudinal trend of the brightness temperature deviation from an ocean model,**
887 **averaged in the alias-free field of view, of V505 (blue line), and corrected value in V620 (red line).**
888

889 ### 6.2.5 Reduced Orbital Variations

890
891 The reduced orbital variations of V620 in the Stokes-1/2 parameter over the ocean have already been
892 introduced and shown in the right panel of Figure 7. What is presented in the left panel of the same
893 figure is the strong orbital variations, of about 2 K peak to peak, that V505 exhibited between
894 ascending and descending passes in the same Stokes-1/2 parameter. These pronounced variations have
895 been reduced in V620 mostly thanks to the optimization and use of the antenna losses measured in orbit
896 **(Section 6.1.6) and the use of only the most stable NIR unit (Section 6.1.5)**.

897 ### 6.2.6 Improved Yearly and Seasonal Stability

898
899 Figure 6 shows the latitudinal, seasonal and yearly variations of the Stokes-1/2 parameter over the
900 ocean. The left plot, for V505, has strong variations with latitude which, as discussed above, have been
901 removed in V620, shown in the right panel. V505 presents also significant seasonal variations, seen as
902 ±2 K alternating blue and red bands in the corresponding **Hovmöller** plot. These strong seasonal

fluctuations have been greatly reduced in V620, down to ±0.4 K**, thanks to the improvement in Section 6.1.6**. In addition, a –0.18 K/year cooling yearly drift is present in V505 data, which has disappeared in V620, for which the trend is of only –0.003 K/year. The long term stability of V620 has further been verified over Antarctica, as presented in Figure 35, which shows the vertical and horizontal brightness temperature at 42° incidence angle measured by SMOS for a period of over 5 years. The fluctuations in horizontal polarization are known to be due to surface roughness fluctuations, being the vertical polarization the best indicator to check for the instrument long term stability. As it can be seen, the yearly drift is indeed negligible.

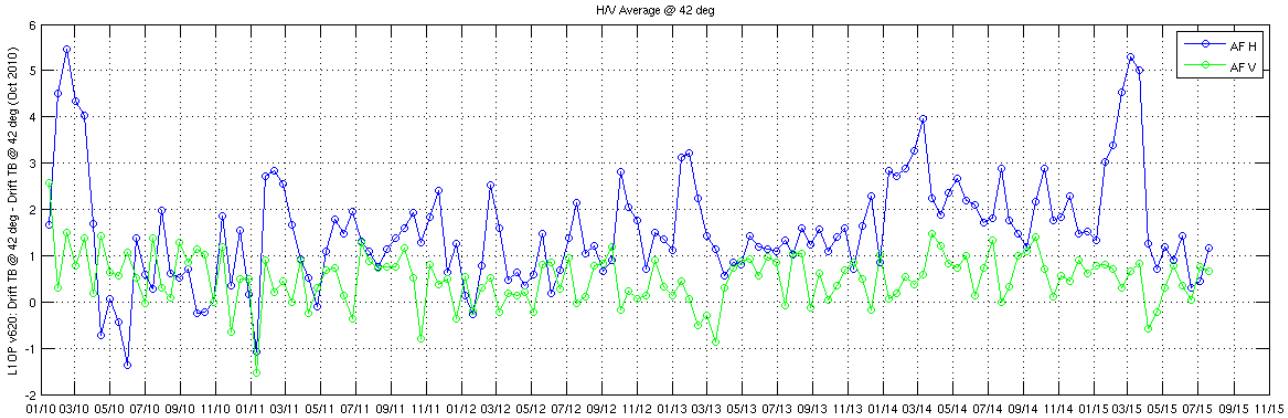

Figure 35: Over 5-year record of vertical and horizontal SMOS brightness temperatures at 42° incidence angle within the Alias-Free Field of View over Antarctica.

7 CURRENT INVESTIGATIONS

Despite the major improvements brought in by V620 version of the SMOS Level-1 processor over the previous version V505 which have been presented, several remaining challenges require further work, in particular, the residual orbital and seasonal variations, including the eclipse season, the further reduction of the spatial ripple and the Sun tails, not to forget the detection and mitigation of RFI effects. This section presents some of the on-going investigations to advance in these directions.

7.1 Level-1 Processor Version V700

As mentioned in the introduction a new version of the processor, V700, has already been delivered, whose major change with respect to the currently operational version V620 is that it can run a so-called 'All-LICEF' mode. The implementation of the All-LICEF mode has, as objective, the simplification of the overall calibration procedure of the MIRAS instrument, to achieve better calibrated measurements and to make faster progress in correcting some of the remaining spatial errors and temporal variations. The concept behind the All-LICEF mode is depicted in Figure 36. The upper part shows the man calibration steps followed in V620: first the NIR radiometers are calibrated using the Cold Sky and an internal matched load, to provide the visibility sample at the origin V(0,0); then NIR is used to calibrate the noise diodes of the on-board Calibration System (CAS); finally the CAS system calibrates all the LICEF receivers of MIRAS. The lower part of Figure 36 shows instead, the much simpler and direct calibration approach of the All-LICEF mode: the LICEF receivers are directly calibrated using the Cold Sky and an internal matched load, and hence, the visibility sample at the origin can be measured by averaging all the calibrated antenna temperatures of the LICEF receivers. The straight advantage of the All-LICEF mode is therefore its extreme simplicity. This mode of operation was already envisaged well before launch, but only the accumulation of 5 years of flight experience allows to properly assessed its performance. It has to be noted that while the Noise Injection Radiometers are intrinsically more stable than the LICEF total power radiometers, the fact that there are 69 of the latter and only 3 of the former (in fact only the most stable NIR unit is currently used), offsets the final result in favour of the All-LICEF solution. To show one example, Figure 37 shows the temporal variations for V620 (left panel) and V700 in All-LICEF mode (right panel), and it can be noticed that the warming trend of 2014 for V620 is not so pronounced in V700. Another illustration of the benefits of the All-LICEF mode is given in Figure 5, where the land-sea contamination correction based on the adjustment of the correlator efficiency coefficients explained earlier has been successfully tested with V700 (right panel) by comparison with the current V620 (left panel) where a significant coastal signature is still

observable. The All-LICEF branch of V700 is undergoing through a detailed assessment before it is accepted for operational use.

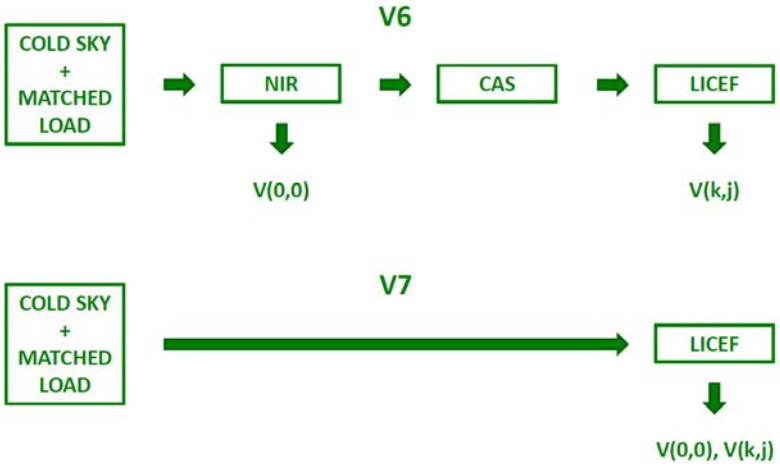

Figure 36: All-LICEF mode

7.2 Beyond V700

Other improvements beyond version V700 are in the pipeline, namely the implementation of an improved Gibbs-2 based image reconstruction algorithm, the further elaboration of improved spatial ripple and Sun mitigation techniques, as well the reduction of residual temporal fluctuations.

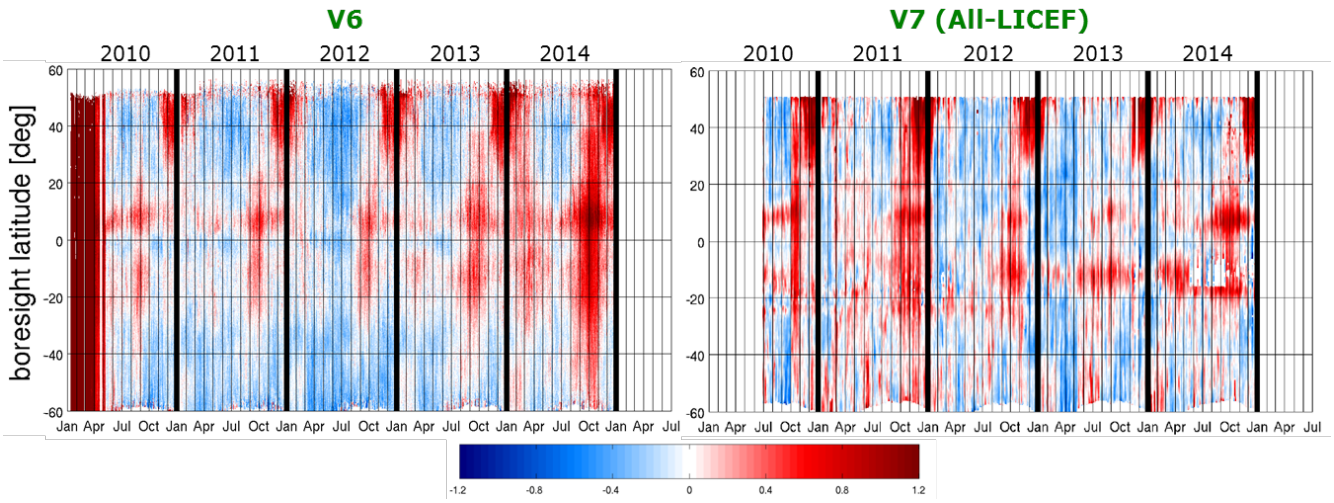

Figure 37: Descending-minus-Ascending pass Stokes-1/2 parameter over the Pacific Ocean, averaged in the alias-free area, with V620 (left) and V700 in All-LICEF mode (right) **–colour scale in Kelvin–**

8 CONCLUSIONS

SMOS mission has passed its extended life time of 5 years and continues to deliver good quality data, with both the MIRAS payload and the PROTEUS platform being in good health. The accumulated data record has allowed continued insight and improvement, from launch till today, of the MIRAS instrument and the Level-1 processor which transforms the visibility measurements into brightness temperature images. This paper has described the results of the detailed investigation of the calibration data and images, in various aspects, including instrumental behaviour and image reconstruction. Special focus has been given to the presentation of the performance of the currently operational version of the Level-1 processor, V620, and its improvements by comparison to the earlier version V505. V620 is a fully polarimetric processor accounting for cross polar terms, with an enhanced image reconstruction technique and based on an improved in-orbit calibration approach which has resulted in overall cleaner and more stable brightness temperature images. Some hints have also been given about on-going investigations with a new processor version already delivered, V700, featuring the All-LICEF mode with a much simpler calibration strategy with potential to reduce the land-sea contamination. Finally, some future avenues, as the Gibbs-2 method, have been mentioned, addressing the still remaining challenges as the residual orbital and seasonal fluctuations, spatial ripple and Sun correction.

9 ACKNOWLEDGEMENTS

The authors would like to express their thanks to Mariano Kornberg with ESA, for providing the long series of instrument parameter values shown in the paper.

10 REFERENCES

Anterrieu E., P. Waldteufel, A. Lannes, (2002), “Apodization Functions for 2-D Hexagonally Sampled Synthetic Aperture Imaging Radiometers”, IEEE Transactions On Geoscience and Remote Sensing, Vol. 40, No. 12, pp.47-51.

Anterrieu E., (2007), “On the Reduction of the Reconstruction Bias in Synthetic Aperture Imaging Radiometry”, IEEE Transactions On Geoscience and Remote Sensing, Vol. 45, No. 3, pp. 592-601.

Anterrieu E., M. Suess, F. Cabot, P. Spurgeon, A. Khazaal, (2015), "An additive mask correction approach for reducing the systematic floor error in imaging radiometry by aperture synthesis", IEEE Geoscience and Remote Sensing Letters, 12(7), pp. 1441-1445.

Brown M.A., F. Torres, I. Corbella, A. Colliander, (2008), "SMOS Calibration", IEEE Transactions On Geoscience And Remote Sensing, Vol. 46, No. 3, 646 – 658.

Camps A., (1996), "Application of Interferometric Radiometry to Earth Observation", PhD Thesis, Polytechnic University of Catalonia.

Camps A., M. Vall-llossera, N. Duffo, M. Zapata, I. Corbella, F. Torres, (2004), "Sun Effects in 2-D Aperture Synthesis Radiometry Imaging and Their Cancelation", IEEE Transactions On Geoscience and Remote Sensing, Vol. 42, No. 6, pp.1161-1167.

Camps A., I. Corbella, F. Torres, N. Duffo, M. Vall-llosera, M. Martín-Neira, (2005), "The Impact of Antenna Pattern Frequency Dependence in Aperture Synthesis Microwave Radiometers", IEEE Transactions On Geoscience and Remote Sensing, Vol. 43, No. 10, pp. 2218-2224.

Camps A., M. Vall-llossera, I. Corbella, N. Duffo, F. Torres, (2008), "Improved Image Reconstruction Algorithms for Aperture Synthesis Radiometers", IEEE Transactions On Geoscience and Remote Sensing, Vol. 46, No. 1, pp.146-158.

Chiuderi Drago F., M. Felli and G. Tofani, 1977, High resolution intensity and polarization structure of the Sun at 21 cm, Astron. Astrophysics. 61, 79-91.

Colliander A., L. Ruokokoski, J. Suomela, K. Veijola, J. Kettunen, V. Kangas, A. Aalto, M. Levander, H. Greus, M. Hallikainen, J. Lahtinen, (2007), "Development and Calibration of SMOS Reference Radiometer", IEEE Transactions On Geoscience and Remote Sensing, Vol. 45, No. 7, pp. 1967–1977.

Colliander, E. Dinnat, D. Le Vine, C.-S. Chae, and J. Kainulainen, 2015, "Assessing long-term stability of SMOS zero-baseline antenna temperature using the Aquarius antenna temperature simulator," Geoscience and Remote Sensing Letters, IEEE, vol. 12, no. 8, pp. 1680-1684.

Corbella I., N. Duffo, M. Vall-llossera, A. Camps, and F. Torres, (2004a), "The visibility function in interferometric aperture synthesis radiometry", IEEE Transactions On Geoscience and Remote Sensing, Vol. 42, No. 8, pp. 1677–1682.

Corbella I., (2004b), "Polarimetric and Extended Formulation of the Visibility Equation". MIRAS Demonstrator Pilot Project 3, MP3-TN-UPC-3000-0002 v1.1, ESA Contract 15138/01/NL/SF.

Corbella I., F. Torres, N. Duffo, M. Martín-Neira, V. González-Gambau, A. Camps, M. Vall-llossera, (2009), "On-Ground Characterization of the SMOS Payload", IEEE Transactions on Geoscience and Remote Sensing, Volume 47, Issue 9, pages: 3123 - 3133.

Corbella I., F. Torres, N. Duffo, I. Durán, M. Pablos, M. Martín-Neira, (2012), "Enhanced SMOS Amplitude Calibration Using External Target", Proceedings of IGARSS-2012, Munich (Germany).

Corbella I., F. Torres, L. Wu, N. Duffo, I. Durán, M. Martín-Neira, (2014), "SMOS Image Reconstruction Errors", poster presented at IGARSS-2014, Quebec (Canada).

Corbella I., L. Wu, F. Torres, N. Duffo, M. Martín-Neira, (2015), "Faraday Rotation Retrieval Using SMOS Radiometric Data", IEEE Transactions On Geoscience and Remote Sensing, Vol. 12, No. 3, pp. 458–461.

Corbella I., I. Duran, L. Wu, F. Torres, N. Duffo, M. Martín-Neira, (in press), "Impact of correlator efficiency errors on SMOS land-sea contamination", submitted to the Transactions on Geoscience and Remote Sensing in January 2015.

Daganzo-Eusebio, E.; Oliva, R.; Kerr, Y. H.; Nieto, S.; Richaume, P.; Mecklenburg, S., (2013), "SMOS Radiometer in the 1400-1427-MHz Passive Band: Impact of the RFI Environment and Approach to Its Mitigation and Cancellation," Geoscience and Remote Sensing, IEEE Transactions on, vol. 51, no. 10, pp. 4999-5007.

Díez-García R., M. Martín-Neira, (2014), "Analysis and Characterization of the Reconstruction Error in Interferometric Synthetic Aperture Imaging Radiometers", MicroRad-2014, Pasadena (California, US).

González-Gambau, V., Turiel, A., Olmedo, E., Martínez, J., Corbella., I., and Camps, A., (2015), 'Nodal sampling: a new image reconstruction algorithm for SMOS', IEEE Transactions on Geoscience and Remote Sensing, in press, doi: 10.1109/TGRS.2015.2499324.

Gourrion J., S. Guimbard, M. Portabella, R. Sabia, (2013), "Toward an Optimal Estimation of the SMOS Antenna-Frame Systematic Errors", IEEE Transactions on Geoscience and Remote Sensing, Vol. 51, No. 9, pp.4752-4760.

Kainulainen J., A. Colliander, (2010), "In-Orbit Performance of the SMOS Reference Radiometers – Results from the Early Commissioning Phase", MicroRad-2010, Washington (US).

Kainulainen J., A. Colliander, J. Closa, M. Martín-Neira, R. Oliva, G. Buenadicha, P. Rubiales-Alcaine, A. Hakkarainen, M. Hallikainen, (2012), "Radiometric Performance of the SMOS Reference Radiometers—Assessment After One Year of Operation", IEEE Transactions on Geoscience and Remote Sensing, vol. 50, no. 5, pp. 1367–1383.

Khazaal A., H. Carfantan, E. Anterrieu, (2009), "On the Reduction of the Systematic Error in Imaging Radiometry by Aperture Synthesis: a New Approach for the SMOS Space Mission", IEEE Transactions on Geoscience and Remote Sensing, Vol. 6, No. 1, pp.47-51.

Khazaal, A., Cabot, F., Anterrieu, E., Soldo, Y. (2014), "A Kurtosis-Based Approach to Detect RFI in SMOS Image Reconstruction Data Processor". IEEE Transactions on Geoscience and Remote Sensing, Volume 52, Issue 11, pp.7038-7047.

Khazaal, A., Leroux, D.J., Cabot, F., Richaume, P., Anterrieu, E., (2015), "Effect of the Polarization Leakage on the SMOS Image Reconstruction Algorithm: Validation Using Ocean Model and In Situ Soil Moisture Data". IEEE Transactions on Geoscience and Remote Sensing, Volume 53, Issue 9, pages: 4961 - 4971.

Lemmetyinen J., J. Uusitalo, J. Kainulainen, K. Rautiainen, N. Fabritius, M. Levander, V. Kangas, H. Greus, J. Pihlflyckt, A. Kontu, S. Kemppainen, A. Colliander, M. Hallikainen, J. Lahtinen, (2007), "SMOS Calibration Subsystem", IEEE Transactions On Geoscience and Remote Sensing, Vol. 45, No. 11, pp. 3691–3700.

Lin W., I. Corbella, F. Torres, N. Duffo, M. Martín-Neira, (2011), "Correction of Spatial Errors in SMOS Brightness Temperature Images", Proceedings of IGARSS-2011, Vancouver (Canada).

Lin Wu, Torres, F., Corbella, I., Duffo, N., Martín-Neira, M., (2012), "Performance of a spatial error correction technique in SMOS brightness temperature images", MicroRad-2012, Villa Mondragone, Tor Vergata University of Rome (Italy).

Lin W., F. Torres, I. Corbella, N. Duffo, I. Durán, M. Vall-llossera, A. Camps, S. Delwart, M. Martín-Neira, (2013), "Radiometric Performance of SMOS Full Polarimetric Imaging", IEEE Geoscience and Remote Sensing Letters, vol 10, Issue 6, pp 1454-1458.

Macelloni, G, Brogioni M., Pettinato, S., Zasso, R. Crepaz, A., Zaccaria, J., Drinkwater, M., (2013), "Ground based L-Band Emission Measurements at DOME-C Antarctica: the DOMEX-2 experiment. IEEE Trans. Geosci. and Remote Sensing, vol 51, No 9, 4718-4730.

Martín-Neira M., S. Ribó, A. J. Martín-Polegre, (2002), "Polarimetric mode of MIRAS," IEEE Transactions on Geoscience and Remote Sensing, vol. 40, no. 8, pp. 1755–1768.

Martín-Neira M., M. Suess, J. Kainulainen, F. Martín-Porqueras, (2008), "The Flat Target Transformation", IEEE Transactions On Geoscience And Remote Sensing, Vol. 46, No. 3, 613 – 620.

Martin-Porqueras F., J. Kainulainen, M. Martín-Neira, I. Corbella, R. Oliva, R. Castro, J. Barbosa, A. Gutierrez, (2010), "Experimental Validation of the Corbella's Visibility Function using HUT-2D and MIRAS", Proceedings of IGARSS-2010, Honolulu, Hawaii (US), pp.4286-4289.

McMullan K., M. Brown, M. Martín-Neira, W. Rits, S. Ekholm, J. Marti and J. Lemanczyk, (2008), "SMOS: The payload", IEEE Transactions On Geoscience and Remote Sensing, Vol. 46, No. 3, 594 – 605.

Mecklenburg Susanne, Matthias Drusch, Yann H. Kerr, Senior Member, IEEE, Jordi Font, Manuel Martín-Neira, Steven Delwart, Guillermo Buenadicha, Nicolas Reul, Elena Daganzo-Eusebio, Roger Oliva, and Raffaele Crapolicchio, (2012), "ESA's Soil Moisture and Ocean Salinity Mission: Mission Performance and Operations", IEEE TGARS, Vol 50, No 5, pages 1354-1366.

Mecklenburg S., M. Drusch, Y. Kerr, J. Font, N. Reul, M. Martín-Neira, R. Oliva, E. Daganzo-Eusebio, J. Fauste, L. Kaleschke, N. Rodriguez-Fernandez, P. de Rosnay, G. Macelloni, J. Muñoz-Sabater, K. Rautiainen, J.P. Grant, N. Verhoest, H. Lievens, P. Richaume, R. Sabia, S. Delwart, R. Crapolicchio, A. de la Fuente, M. Kornberg, (in press), "ESA's Soil Moisture and Ocean Salinity Mission: from Science to Operational Applications". This RSE special issue, submitted.

Oliva R., E. Daganzo, Y. Kerr, S. Mecklenburg, S. Nieto, P. Richaume, C. Gruhier, (2012), "SMOS Radio Frequency Interference Scenario: Status and Actions Taken to Improve the RFI Environment in the 1400-1427 MHz Passive Band". IEEE Trans Geosci. Remote Sens., Special issue on Soil Moisture and Ocean Salinity Mission. Vol. 50, No 5, pp. 1427-1439.

Oliva R., M. Martín-Neira, I. Corbella, F. Torres, J. Kainulainen, J.E. Tenerelli, F. Cabot, F. Martin-Porqueras, (2013), "SMOS Calibration and Instrument Performance after One Year in Orbit", IEEE Transactions on Geoscience and Remote Sensing, Vol. 51, No 1, pp. 654-670.

Oliva R., E. Daganzo, Y. Soldo, Y. Kerr, F. Cabot, P. Richaume, E. Anterrieu, A. Gutierrez, J. Barbosa, G. Lopes, (in press), "Status of RFI in the 1400-1427 MHz passive band: The SMOS perspective", This RSE special issue, submitted.

Rubiales P., J. Closa, E. Checa, S. Dolce, M. Kornberg, M. Martín-Neira, (2015), "SMOS Payload Thermal Control: Review of performances after 5 years in orbit operation", 45th International Conference on Environmental Systems, Bellevue, Washington (US).

SMOS Level 2 Ocean Salinity Team, "SMOS L2 Ocean Salinity Algorithm Theoretical Baseline Document", ARGANS, SO-TN-ARG-GS-0007_L2OS-ATBD_v3.12_150731, July 2015.

Torres F., I. Corbella, A. Camps, N. Duffo, M. Vall-llossera, S. Beraza, C. Gutierrez, M. Martín-Neira, (2006), "Denormalization of Visibilities for In-Orbit Calibration of Interferometric Radiometers", IEEE Transactions on Geoscience and Remote Sensing. Vol. 44, No. 10, pp.2679-2686.

Torres F., I. Corbella, L. Wu, N. Duffo, J. Gourrion, J. Font, M. Martín-Neira, (2012), "Minimization of Image Distortion in SMOS Brightness Temperature Maps Over the Ocean", GeoScience and Remote Sensing Letters, Vol. 9, No. 1, pp.18-22.

Torres F., I. Corbella, I. Duran, W. Lin, N. Duffo, M. Martín-Neira, (2014), "Residual Calibration Error Impact On SMOS SLL Performance", IGARSS-2014 Proceedings, pp.2542–2545, Quebec (Canada).

Torres F., I. Corbella, L. Wu, N. Duffo, S. Delwart, M. Martín-Neira, (2015), "In-Orbit Validation of SMOS Full Polarimetric Equations", IEEE Geoscience and Remote Sensing Letters, Vol. 12, Issue 3, pp.458-461.